Chiral chaos–enhanced sensing

Yun-Qiu Ge,[1,2,‡] Zhe Wang,[3,‡] Qian-Chuan Zhao,[3] Jing Zhang,[4,5,*] and Yu-xi Liu[1,2,†]

[1] *School of Integrated Circuits, Tsinghua University, 100084 Beijing, China*
[2] *Frontier Science Center for Quantum Information, 100084 Beijing, China*
[3] *Department of Automation, Tsinghua University, 100084 Beijing, China*
[4] *School of Automation Science and Engineering, Xi'an Jiaotong University, Xi'an, 710049 Shaanxi, China*
[5] *MOE Key Laboratory for Intelligent Networks and Network Security, Xi'an Jiaotong University, Xi'an, 710049 Shaanxi, China*

(Received 18 April 2024; revised 30 September 2024; accepted 29 January 2025; published 13 February 2025)

"Chirality" refers to the property that an object and its mirror image cannot overlap each other by spatial rotation and translation. Chirality can be found in various research fields. Here we propose chiral chaos and design a chiral chaotic device using whispering gallery mode resonators and tips, where the routes to chaos exhibit pronounced chirality for two pumping directions. The mechanism underlying chirality is that time-reversal symmetry of traveling-wave light fields is regulated by tips, and chaos originates from the nonlinear optomechanical interactions. We propose metrics based on the Lyapunov exponents to quantify the symmetry and chirality between routes to chaos. We show that the proposed chiral chaotic device can be applied to achieve sensing with high sensitivity, a broad detectable range, and strong robustness regarding phase and orientation randomness of weak signals. Our work provides a promising candidate for on-chip sensing and may have applications in chaotic networks and chaotic communications.

DOI: 10.1103/PhysRevApplied.23.024034

I. INTRODUCTION

The concept of chirality has permeated many branches of science, such as biological sciences [1], chemistry [2,3], soft matter physics [4], particle physics [5], and optics [6,7]. Over the past few decades, research on chiral behaviors has deeply fascinated researchers [4,8]. Considerable efforts have been devoted to the study of chirality in light-matter interactions [9,10], and the value of chiral products and chiral devices generated from such efforts has been widely recognized in relevant application areas. Representative examples include enantiosensitive control [11], optofluidic sorting of particles [12], negative refractive index materials [13], and novel optical tools [14,15]. The interactions between light and matter can occur in diverse forms, including radiation pressure, scattering, emission, and absorption. As the light intensity increases, many of these interactions are accompanied by nonlinear effects [16].

Chaos is a nonlinear phenomenon that can be observed in most nonlinear systems. It describes certain dynamics that are extremely sensitive to initial conditions, and has broad applications in engineering [17]. Recently, research on chaos using radiation pressure–based nonlinear systems, i.e., optomechanical systems in which optical and mechanical modes interact via radiation pressure, has attracted widespread attention [18–21]. Various radiation pressure–based systems provide ideal platforms for studying nonlinear physics and chaos, e.g., whispering gallery mode (WGM) resonators, Fabry-Pérot cavities, and microwave optomechanical resonators [22]. A series of intriguing chaotic phenomena in optomechanical systems have been proposed and observed, including intermittent chaos [23], nonreciprocal chaos [24], parity-time-symmetry-breaking chaos [25], and anti-parity-time-symmetry-breaking chaos [26]. Although chiral behaviors and chaotic dynamics have been studied in nonlinear light-matter interaction systems from multiple aspects, the intersection between chirality and chaos remains unexplored. This intersection may advance the applications of chaos and broaden chaos theory.

The development of microfabrication and nanofabrication techniques has enabled the miniaturization of chaotic devices based on radiation pressure interactions to the micron level [22]. This opens up new possibilities for developing high-precision sensors [27–31] by the use of these miniaturized nonlinear devices. Chaotic sensors

*Contact author: zhangjing2022@xjtu.edu.cn
†Contact author: yuxiliu@mail.tsinghua.edu.cn
‡These authors contributed equally to this work.

work mainly by using an abrupt change in observables before and after the order-chaos phase transitions [32–34]. Such a working principle has the advantages of high sensitivity, fast response, and good reliability, but its practicality is severely limited by the types of detected signals [30]. For uncontrolled signals, e.g., mechanical displacements with uncertain directions and optical signals with random phases or frequencies, even if their amplitudes exceed the critical threshold of order-chaos phase transitions, the corresponding observables may not exhibit abrupt changes [35–37]. Thus, during the sensing process, the response of chaotic sensors to certain signals may become too weak to capture them accurately, resulting in false negative errors. These errors are difficult to avoid and hinder the applications of chaotic sensors. Based on the chirality in chaotic dynamics, we propose a more efficient sensing principle that can reduce the occurrence of false negative errors and thus enhance chaotic sensing.

In this paper, by our using coupled WGM resonators as the controlled object and tips as controllers, we propose a controllable chiral chaotic device that supports both optical and mechanical modes. The tips are nanoscale probes made from optical fibers and are commonly used for tuning the frequency, scattering, and dissipation of optical resonators [38]. Chaos in this device originates from the nonlinear interactions between optical and mechanical modes via radiation pressure. The device is pumped via a tapered fiber with two ports. We find that for pumping from two opposite ports of the tapered fiber, the corresponding tip-controlled chaotic dynamics exhibit chirality along the axis of the scattering phase φ. We demonstrate that the tip-controlled scattering phase φ between optical modes can nontrivially regulate time-reversal symmetry of the system, thereby inducing chiral chaos. To quantify the degree of chirality and symmetry in chaotic dynamics, we design metrics based on the Lyapunov exponents. Besides, we propose a new sensing principle based on chiral chaos, i.e., we construct the sensing window that is sensitive to weak signals. Through a series of evaluations and comparisons, we demonstrate that the proposed sensing method is superior to the conventional chaotic sensing method in sensing performance.

This paper is organized as follows. In Sec. II, we introduce the theoretical model to describe the proposed chiral chaotic device and the Hamiltonian, and the corresponding equations of motion are derived. In Sec. III, the phase diagrams corresponding to different pumping ports are presented, and the chiral chaos phenomenon is shown. Moreover, we propose two metrics and demonstrate how to apply them to quantitatively characterize the degree of symmetry and chirality between different routes to chaos. In Sec. IV, we illustrate how to utilize the chiral chaotic device to perform high-precision sensing, and demonstrate its superiority. Finally, we summarize the main results, and further discuss the potential applications and experimental feasibility of the proposed device in Sec. V.

II. CHIRAL CHAOTIC DEVICE

As schematically shown in Fig. 1(a), the proposed chiral chaotic device consists of a vibrating WGM microtoroid resonator A and a nonvibrating WGM microtoroid resonator B. Thus, resonator A is an optomechanical system [39,40], and resonator B is only an optical system. There are surface defects in resonator A as schematically shown in Fig. 1(a) as a protrusion. Two tips acting as Rayleigh scatterers contact the rim of resonator B. To avoid non-Rayleigh-scattering effects, we require that the effective size of the fiber tips should be much smaller than the wavelength of optical modes in resonator B. The two resonators are coupled to each other via the overlapping evanescent fields between the resonators [41]. The evanescent fields are the electromagnetic fields that extend beyond the physical boundaries of the resonators and decay exponentially with the distance from the surface. We assume that each resonator supports two counterpropagating optical modes [42], i.e., the clockwise (CW) and counterclockwise (CCW) optical modes. $\hat{a}_{\mathrm{CW}}$ and $\hat{b}_{\mathrm{CW}}$ are defined as the annihilation operators for CW optical modes in resonator A and resonator B, respectively. $\hat{a}_{\mathrm{CCW}}$ and $\hat{b}_{\mathrm{CCW}}$ are defined as the annihilation operators for CCW optical modes in resonator A and resonator B, respectively. We further assume that $\hat{a}_{\mathrm{CW}}$ and $\hat{a}_{\mathrm{CCW}}$ modes have the same resonance frequency ω_{A} and damping rate κ, and that $\hat{b}_{\mathrm{CW}}$ and $\hat{b}_{\mathrm{CCW}}$ modes have the same resonance frequency ω_{B} and damping rate γ. The CW and CCW modes in resonator A can be coupled only to the CCW and CW modes, respectively, in resonator B via the overlapping evanescent fields. The mechanical mode in resonator A can be described by the displacement operator $\hat{q}$ and the momentum operator $\hat{p}$ with mechanical frequency Ω and damping rate Γ. We ignore the mechanical effects in resonator B due to its relatively low quality factor and the suppression of mechanical oscillation caused by the contact of the two tips. The nonlinear optomechanical interaction [22] between the optical modes and the mechanical mode in resonator A is written as $\hbar G(\hat{a}_{\mathrm{CW}}^{\dagger}\hat{a}_{\mathrm{CW}} + \hat{a}_{\mathrm{CCW}}^{\dagger}\hat{a}_{\mathrm{CCW}})\hat{q}$, with the single-photon optomechanical coupling strength $G = (\omega_{\mathrm{A}}/R) \times \sqrt{\hbar/m\Omega}$, where R and m are the radius and effective mass of resonator A, respectively. We also assume that a tapered fiber with two ports is evanescently coupled to resonator A. Thus, the pumping field can be applied to the device through either port 1 or port 2. In the rotating reference frame with pumping field frequency ω, the Hamiltonian of the proposed chiral chaotic device is given by ($\hbar = 1$)

$$\hat{H} = \hat{H}_0 + \hat{H}_{\mathrm{OM}} + \hat{H}_{\mathrm{I}} + \hat{H}_{\mathrm{P}}, \tag{1a}$$

$$\hat{H}_0 = \Delta_A(\hat{a}^\dagger_{CW}\hat{a}_{CW} + \hat{a}^\dagger_{CCW}\hat{a}_{CCW}) + \frac{\Omega}{2}(\hat{p}^2 + \hat{q}^2) + \Delta_B(\hat{b}^\dagger_{CW}\hat{b}_{CW} + \hat{b}^\dagger_{CCW}\hat{b}_{CCW}), \tag{1b}$$

$$\hat{H}_{OM} = -G(\hat{a}^\dagger_{CW}\hat{a}_{CW} + \hat{a}^\dagger_{CCW}\hat{a}_{CCW})\hat{q} \tag{1c}$$

$$\hat{H}_I = -J(\hat{a}^\dagger_{CW}\hat{b}_{CCW} + \hat{a}^\dagger_{CCW}\hat{b}_{CW} + \text{H.c.}) - (\eta\hat{a}^\dagger_{CW}\hat{a}_{CCW} + |\xi|e^{i\varphi}\hat{b}^\dagger_{CW}\hat{b}_{CCW} + \text{H.c.}), \tag{1d}$$

$$\hat{H}_P = \begin{cases} i\varepsilon(\hat{a}^\dagger_{CW} - \hat{a}_{CW}), & \text{pumping from port 1,} \\ i\varepsilon(\hat{a}^\dagger_{CCW} - \hat{a}_{CCW}), & \text{pumping from port 2,} \end{cases} \tag{1e}$$

where $\Delta_A = \omega_A - \omega$, $\Delta_B = \omega_B - \omega$, $\hat{H}_0$ denotes the free Hamiltonian of the vibrating mechanical mode in resonator A and the optical modes in both resonators, and $\hat{H}_{OM}$ denotes the optomechanical interaction Hamiltonian for the mechanical mode and the optical modes in resonator A.

The couplings between optical modes in the resonators are illustrated in Fig. 1(b) and are described by the interaction Hamiltonian $\hat{H}_I$. Here, η denotes the backscattering-induced coupling strength between CCW and CW modes in resonator A caused by surface defects [43], $|\xi|e^{i\varphi}$ and $|\xi|e^{-i\varphi}$ denote the complex scattering strength between WGMs in resonator B caused by the two tips; the details for the expressions of $|\xi|$ and φ can be found in Appendix A. In current experiments [44–46], $|\xi|$ and φ can be adjusted by one moving the fiber tips in three-dimensional space or electroplating the surface of the tips with various materials. The green region in Fig. 1(c) shows the range of scattering parameters $|\xi|$ and φ achievable by one varying the relative position (i.e., the spatial phase difference β in resonator B) and geometric scale of the two tips. J represents the coupling strength between the resonators, which is determined by the effective distance between the resonators. Besides, through a tapered fiber, in which the tapered region of the tapered fiber surrounds a stronger evanescent field that couples to the optical mode in resonator A, the monochromatic pumping field with frequency ω can be applied to the optical modes in resonator A, as shown schematically in Fig. 1(a) and in Eq. (1e). The interaction Hamiltonian between the optical mode in resonator A and the pumping field applied through either port 1 or the port 2 is described via the Hamiltonian $\hat{H}_P$, where ε describes the coupling strength between the optical mode and the pumping field. Under the current experimental conditions [38,44,46], the positions of the resonators, the tapered fiber, and the tips can be precisely controlled by nanopositioning translation stages and other methods. Thus, J, $|\xi|$, and φ can be flexibly adjusted within a wide range, and the proposed device is highly controllable.

Dynamics of the chiral chaotic device are described by the Heisenberg equations of motion. For the convenience

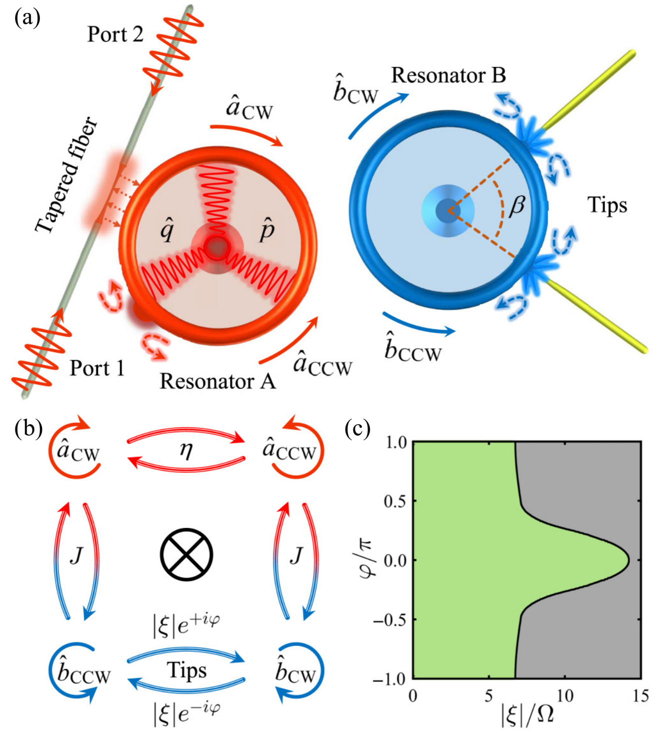

FIG. 1. (a) The proposed chiral chaotic device, where an optomechanical resonator A is coupled to an optical resonator B, and two tips acting as Rayleigh scatterers contact the rim of resonator B. Here, each resonator supports CW and CCW optical modes. Through the overlap of evanescent fields of optical modes, the CW and CCW modes in resonator A are coupled to the CCW and CW modes, respectively, in resonator B. Resonator A also supports a mechanical mode, which interacts with the optical modes via radiation pressure. Additionally, resonator A has with a protrusion on its rim, which indicates the surface defects. The tapered fiber with two pumping ports is evanescently coupled to resonator A. (b) Loops composed of optical modes and the interactions among them. (c) Under common experimental conditions, the ability of the tips to tune the scattering strength $|\xi|$ and scattering phase φ (see Appendix A for details). Green and gray regions show achievable and unachievable parameter ranges, respectively.

of solving them, we replace all operators with their expectation values, i.e., $\hat{o} \Rightarrow \langle\hat{o}\rangle = o$, where $\hat{o}$ represents any operator. Moreover, in the limit of large photon numbers, we apply the semiclassical approximation to ignore the correlations between optical and mechanical modes [47,48]. Then the equations of motion can be obtained as (we use pumping from port 1 as an example)

$$\dot{a}_{CW} = (-i\Delta^q_A - \kappa)a_{CW} + i\eta a_{CCW} + iJb_{CCW} + \varepsilon, \tag{2a}$$

$$\dot{a}_{CCW} = (-i\Delta^q_A - \kappa)a_{CCW} + i\eta a_{CW} + iJb_{CW}, \tag{2b}$$

$$\dot{q} = \Omega p, \quad \dot{p} = -\Omega q + G(|a_{CW}|^2 + |a_{CCW}|^2) - \Gamma p, \tag{2c}$$

$$\dot{b}_{\mathrm{CW}} = (-i\Delta_{\mathrm{B}} - \gamma)b_{\mathrm{CW}} + i|\xi|e^{i\varphi}b_{\mathrm{CCW}} + iJa_{\mathrm{CCW}}, \quad (2d)$$

$$\dot{b}_{\mathrm{CCW}} = (-i\Delta_{\mathrm{B}} - \gamma)b_{\mathrm{CCW}} + i|\xi|e^{-i\varphi}b_{\mathrm{CW}} + iJa_{\mathrm{CW}}, \quad (2e)$$

with $\Delta_{\mathrm{A}}^{q} = \Delta_{\mathrm{A}} - Gq$, i.e., the resonance frequency of optical modes in resonator A is modulated by mechanical oscillations.

III. CHIRAL CHAOS AND ITS METRICS

We now numerically solve the equations of motion, i.e., Eqs. (2a)–(2e), to obtain the dynamics of the system. To simplify the discussion, we normalize all frequency scales to the mechanical oscillation frequency Ω and extend the timescale to $\tau = \Omega t$. Moreover, in all figures, we discard the initial transient state $\tau/2\pi \in [0, 4096]$. Figures 2(a) and 2(b) depict the phase diagrams of the device for pumping from port 1 and port 2, respectively. The green, red, and black regions in the phase diagrams correspond to the device working in the self-induced-oscillation, period-doubling-bifurcation, and chaotic regimes, respectively. In optomechanical systems, self-induced oscillation occurs when the optical radiation pressure force provides sufficient energy to overcome mechanical damping; this results in sustained periodic oscillation of the mechanical mode. As the parameters vary, the system can undergo period-doubling bifurcations, a type of transition in which stable oscillatory states evolve into more complex states with doubled periods. The cascade of such bifurcations can ultimately lead to chaos, a state that exhibits extreme sensitivity to initial conditions and unpredictable long-term behavior [20,21]. Different regimes in the phase diagrams are classified on the basis of the maximal Lyapunov exponent $\lambda_{\max}$ (for chaos, $\lambda_{\max} > 0$; for order, $\lambda_{\max} < 0$) and the frequency spectrum of the mechanical oscillations [50,51]. Thus, it is clear that the sign of $\lambda_{\max}$ is enough to establish if a system is chaotic or not chaotic. Figures 2(a) and 2(b) show that these two phase diagrams are chiral along the φ axis. With the continuous increase of φ from $-\pi$ to π, the transition process between the ordered regime and the chaotic regime for pumping from port 2 is the reverse of that for pumping from port 1. We point out that by one tuning $|\xi|$ and φ, which corresponds to one adjusting the fiber tips, the working state of the chiral chaotic device can be flexibly switched. The structure properties of the bifurcation diagrams in Figs. 2(c) and 2(d) show that chiral chaos can be induced by one tuning the scattering phase φ. As illustrated in the lower panels in Figs. 2(c) and 2(d), the value distributions of $\lambda_{\max}$ on the φ axis, especially the position of periodic windows in the chaotic regime, also provide evidence to support this conclusion. We note that the two phase diagrams exhibit no chirality along the $|\xi|$ axis; therefore, $|\xi|$ is not the key factor to achieve chiral chaos (more details can found in Appendix B).

Physically, the chiral chaotic dynamics in Fig. 2 shows that the time-reversal symmetry of the device is regulated by φ. As illustrated in Fig. 1(b), photons hopping along two reverse loops accumulate opposite net phases, i.e., hopping along the loop $\hat{a}_{\mathrm{CCW}} \rightarrow \hat{b}_{\mathrm{CW}} \rightarrow \hat{b}_{\mathrm{CCW}} \rightarrow \hat{a}_{\mathrm{CW}} \rightarrow \hat{a}_{\mathrm{CCW}}$

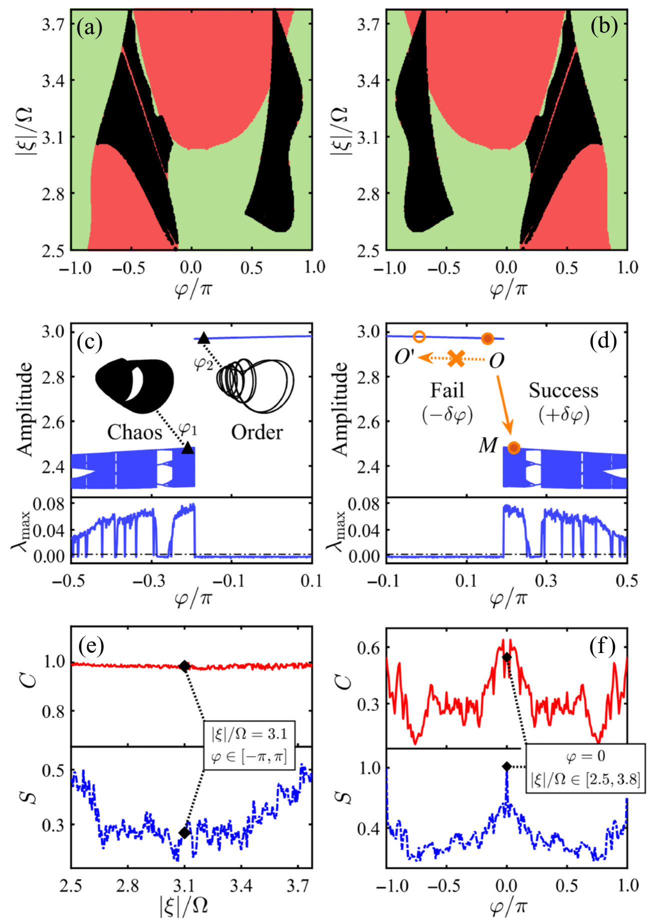

FIG. 2. (a),(b) Phase diagrams of the device for two different pumping directions, where (a),(b) correspond to pumping from port 1 and port 2, respectively, as shown in Fig. 1(a) and Eq. (1e). The green, red, and black regions represent the self-induced-oscillation, period-doubling-bifurcation, and chaotic regimes, respectively. (c),(d) Bifurcation diagrams (upper panels) of the mechanical oscillation amplitude versus φ, and the corresponding maximal Lyapunov exponent $\lambda_{\max}$ spectra (lower panels), in which the dash-dotted black lines mark $\lambda_{\max} = 0$. (c),(d) correspond to pumping from port 1 and port 2, respectively. The insets in (c) present the phase-space trajectories of the light intensity I_{A} ($I_{\mathrm{A}} = |a_{\mathrm{CW}}|^2 + |a_{\mathrm{CCW}}|^2$) in resonator A, where $\varphi_1 = -0.2\pi$ (chaos) and $\varphi_2 = -0.18\pi$ (order). The insets in (d) show the chaotic sensing principle $O \rightarrow M$, and the false negative error $O \rightarrow O'$. (e),(f) The chirality C and symmetry S between the dynamics in (a),(b). For given $|\xi|$, the two chaotic dynamics correspond to $\varphi \in [-\pi, \pi]$ in (a),(b); for given φ, the two chaotic dynamics correspond to $|\xi|/\Omega \in [2.5, 3.8]$ in (a),(b). The parameters are as follows [22,49]: $\Omega = 2\pi \times 20$ MHz, $\Delta_{\mathrm{A}}/\Omega = \Delta_{\mathrm{B}}/\Omega = -0.5$, $\varepsilon/\Omega = 5.8 \times 10^4$, $J/\Omega = 2$, $\gamma/\Omega = 5$, $G/\Omega = 5 \times 10^{-5}$, $\eta/\Omega = 0.15$, $\Gamma/\Omega = 5 \times 10^{-3}$, $\kappa/\Omega = 0.25$, in (c),(d), $|\xi|/\Omega = 3$.

and the reverse loop $\hat{a}_{\mathrm{CCW}} \rightarrow \hat{a}_{\mathrm{CW}} \rightarrow \hat{b}_{\mathrm{CCW}} \rightarrow \hat{b}_{\mathrm{CW}} \rightarrow \hat{a}_{\mathrm{CCW}}$, they accumulate the net phases $-\varphi$ and φ, respectively. Applying the gauge transformation and the time-reversal transformation [52,53], we find that once $\varphi \neq \mathbb{Z}\pi$, where $\mathbb{Z}$ denotes an arbitrary integer, the light fields in the device no longer have time-reversal symmetry (see Appendix C). Moreover, the net hopping phase indicates the existence of a static optical gauge field, which can be equivalent to a magnetic field for photons [54,55]. The gauge field has nontrivial effects on the working states of the device [56], e.g., regulation of time-reversal symmetry of the entire device. To demonstrate this, we calculate the steady-state light intensities in the device. For simplicity, we show only the light intensities ($I_{\mathrm{A}}^{\mathrm{s}} = |a_{\mathrm{CW}}^{\mathrm{s}}|^2 + |a_{\mathrm{CCW}}^{\mathrm{s}}|^2$) in resonator A, which can be written as

$$
\begin{aligned}
I_{\mathrm{A},1}^{\mathrm{s}} &= g(|\widetilde{\Delta}_{\mathrm{A}}|^2 + |\eta + Fe^{i\varphi}|^2), \quad \text{pumping from port 1,} \\
I_{\mathrm{A},2}^{\mathrm{s}} &= g(|\widetilde{\Delta}_{\mathrm{A}}|^2 + |\eta + Fe^{-i\varphi}|^2), \quad \text{pumping from port 2,}
\end{aligned}
\tag{3}
$$

in which the specific expressions for g, $\widetilde{\Delta}_{\mathrm{A}}$, and F can be found in Appendix D. Then, we obtain the light intensity difference in resonator A generated by pumping from two different ports, i.e.,

$$
\delta I_{\mathrm{A}}^{\mathrm{s}} = I_{\mathrm{A},1}^{\mathrm{s}} - I_{\mathrm{A},2}^{\mathrm{s}} = g(|\eta + Fe^{i\varphi}|^2 - |\eta + Fe^{-i\varphi}|^2). \tag{4}
$$

We can find that for the trivial gauge phase, i.e., $\varphi = \mathbb{Z}\pi$, $I_{\mathrm{A},1}^{\mathrm{s}} = I_{\mathrm{A},2}^{\mathrm{s}}$ and $\delta I_{\mathrm{A}}^{\mathrm{s}} = 0$, while for the nontrivial gauge phases, i.e., $\varphi \neq \mathbb{Z}\pi$, the value distribution of $\delta I_{\mathrm{A}}^{\mathrm{s}}$ on the φ axis exhibits chirality. One can verify that $I_{\mathrm{A},1}^{\mathrm{s}} \Rightarrow I_{\mathrm{A},2}^{\mathrm{s}}$ and $\delta I_{\mathrm{A}}^{\mathrm{s}} \Rightarrow -\delta I_{\mathrm{A}}^{\mathrm{s}}$, under the transformation of $\varphi \Rightarrow -\varphi$, which is the origin of chirality. For chaotic states, we can define a similar light intensity difference $\delta I_{\mathrm{A}}^{\mathrm{c}}$. Although the analytical expression for $\delta I_{\mathrm{A}}^{\mathrm{c}}$ is unobtainable [57], the φ-dependent chirality on $\delta I_{\mathrm{A}}^{\mathrm{c}}$ is the same as that on $\delta I_{\mathrm{A}}^{\mathrm{s}}$, as shown in the numerical results in Appendix B.

We note that existing chiral parameters [58,59] are not suitable for characterizing and quantifying the degree of chirality in chaotic dynamics. To address this, we propose a new metric to quantify chirality. Besides the chiral metric, we also propose the corresponding metric for symmetry in chaotic dynamics. Both metrics are used to describe related "geometric" properties between different parameter-dependent evolution processes, e.g., routes to chaos under different conditions. Combined with the maximal Lyapunov exponent $\lambda_{\max}$ spectra, we provide geometric interpretations for both the chirality and the symmetry. As schematically illustrated in Fig. 3, the two parameter-dependent evolution processes are reflected in the $\lambda_{\max}$ spectra as two curves (red and blue curves). Thus, the geometric symmetry and geometric chirality between the blue and red curves can be regarded as the symmetry and chirality (equivalent) between the corresponding two parameter-dependent evolution processes, respectively. We emphasize here that the value of $\lambda_{\max}$ is extremely sensitive to the changes in parameters of the nonlinear differential or map equations, e.g., Eqs. (2a)–(2e), and is also related to the algorithms [60,61]. The sign (i.e., + or −) of $\lambda_{\max}$ is opposite for the ordered ($\lambda_{\max} < 0$) and chaotic ($\lambda_{\max} > 0$) regimes, which shows excellent distinguish ability, as shown in Fig. 3.

To quantitatively characterize the degree of symmetry and chirality between different routes to chaos, we design the following metrics based on the Lyapunov exponents. We first define x as the parameter condition under which the system is in state U with the maximal Lyapunov exponent $\lambda_{\max}$. If we assign N such parameter conditions to set $\{x_i\}$ according to certain rules, then we can obtain a parameter-dependent evolution process $\{U_i\}$ of the system and the corresponding parameter-dependent maximal Lyapunov exponent spectrum $\{\lambda_{\max}^i\}$, $i = 1, 2, \ldots, N$. We emphasize that we are specifically discussing Lyapunov exponent spectra based on parameter-dependent evolution processes, rather than those based on time-dependent evolution processes. For an N-element parameter-dependent maximal Lyapunov exponent spectrum, the index i corresponds to the ith parameter. Similarly, we create another N-element condition set $\{y_i\}$, and obtain the corresponding parameter-dependent evolution process $\{V_i\}$ and the maximal Lyapunov exponent spectrum $\{\Lambda_{\max}^i\}$, $i = 1, 2, \ldots, N$. For the symmetry metric S, to quantify the "geometric symmetry" between the two N-element parameter-dependent maximal Lyapunov exponent spectra, we compare elements with symmetric indices in the two spectra, i.e., the symmetry pair (i, i). For the chirality metric C, to quantify the "geometric chirality" between the two N-element parameter-dependent maximal Lyapunov exponent spectra, we compare elements with mirror image indices in the two spectra, i.e., the chiral pair $(i, N - i + 1)$. Then the metrics S and C can be defined as

$$
S = 1 - \frac{1}{N} \sum_{i=1}^{N} \frac{|\lambda_{\max}^i - \Lambda_{\max}^i|}{|\lambda_{\max}^i| + |\Lambda_{\max}^i|}, \tag{5}
$$

$$
C = 1 - \frac{1}{N} \sum_{i=1}^{N} \frac{|\lambda_{\max}^i - \Lambda_{\max}^{N-i+1}|}{|\lambda_{\max}^i| + |\Lambda_{\max}^{N-i+1}|}. \tag{6}
$$

Our definition of the metrics S and C provides a continuous measure in the range $[0, 1]$. Moreover, we emphasize that for S and C, the signs (i.e., + or −) of $\{\lambda_{\max}^i\}$ and $\{\Lambda_{\max}^i\}$ are crucial, while their specific values are also important. Such metrics imply that we regard chaos and order as two completely opposite or completely asymmetrical states, but do not make further distinctions. This

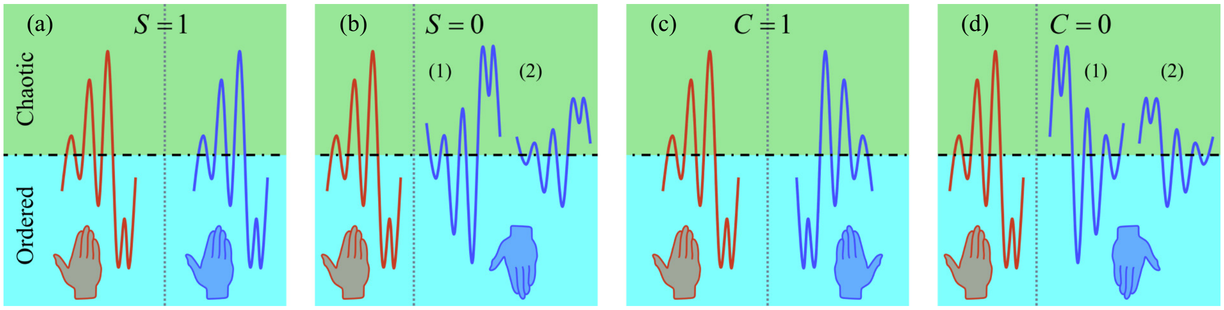

FIG. 3. Geometric interpretations for the metrics S and C. All the red and blue curves represent N-element parameter-dependent maximal Lyapunov exponent spectra. The dash-dotted black lines represent $\lambda_{\max} = 0$, and the green and cyan regions separated by them represent the chaotic regimes ($\lambda_{\max} > 0$) and the ordered regimes ($\lambda_{\max} < 0$), respectively. In all panels, the red and blue curves represent the $\lambda_{\max}$ spectra for the corresponding extreme cases, i.e., S and C reach 0 or 1. In (b), two different types of blue curve are labeled as "(1)" and "(2)," both of which satisfy the requirement of being completely asymmetrical ($S = 0$) with respect to the red curve on the left. In (d), two different types of blue curve are labeled as "(1)" and "(2)", both of which satisfy the requirement of being completely achiral ($C = 0$) with respect to the red curve on the left. Here, the arrangements of the red and blue hands at the bottom indicate the structural features of the corresponding S or C.

means that all ordered states (e.g., self-induced oscillation and period-doubling bifurcations) are completely asymmetric to all chaotic states (e.g., chaos, hyperchaos, and intermittent chaos [57]). The metrics S and C integrate sign-based classification with parameter-dependent maximal Lyapunov exponent spectra, providing a quantitative approach to measuring chirality and symmetry in chaotic dynamics.

We now clarify the basic working principles underlying the two metrics: (1) If the two parameter-dependent evolution processes exhibit the same properties under two different sets of parameter conditions, i.e., the distributions of chaotic states and ordered states are exactly the same, then the two sets of conditions are regarded as equivalent, and the corresponding two evolution processes are ideally symmetrical. (2) If the two parameter-dependent evolution processes are mirror images of each other under two different sets of parameter conditions, i.e., the distributions of chaotic states and ordered states are chiral [see Figs. 2(c) and 2(d) or Appendix B], then the two sets of conditions are regarded as "enantiomers" and the corresponding two evolution processes are ideally chiral. The values of C and S, i.e., the value distributions of $\{\lambda^i_{\max}\}$ and $\{\Lambda^i_{\max}\}$, reflect the chirality and symmetry between $\{U_i\}$ and $\{V_i\}$. As shown in Fig. 3(a), if the two parameter-dependent evolution processes are ideally symmetrical, i.e., $U_i = V_i$, then $\lambda^i_{\max} = \Lambda^i_{\max}$ (the red and blue curves are exactly the same) and $S = 1$. In contrast, as shown in Fig. 3(b), if the two parameter-dependent evolution processes are completely asymmetrical, i.e., the states of U_i and V_i are completely opposite (one is ordered and the other is chaotic), then $\Phi(\lambda^i_{\max}) \neq \Phi(\Lambda^i_{\max})$ and $S = 0$, where $\Phi(X)$ is the Heaviside function [for $X > 0$, $\Phi(X) = 1$; for $X < 0$, $\Phi(X) = 0$]. We note that the condition for $S = 1$ is stricter than that for $S = 0$.

For the parameter-dependent evolution process described by the red curve in Fig. 3, there exists only one type of evolution process that is ideally symmetrical with it, i.e., the blue curve in Fig. 3(a), while there exists a series of evolution processes that are completely asymmetrical with it, e.g., the blue curves (1) and (2) in Fig. 3(b). Similarly, as shown in Fig. 3(c), if the two parameter-dependent evolution processes are ideally chiral, i.e., $U_i = V_{N-i+1}$, then $\lambda^i_{\max} = \Lambda^{N-i+1}_{\max}$ and $C = 1$. In this special case, for the evolution process described by the red curve, there exists only one evolution process, i.e., the blue curve in Fig. 3(c), that is ideally chiral with it. For the special case $C = 0$, the two parameter-dependent evolution processes $\{U_i\}$ and $\{V_i\}$ are completely achiral, i.e., one of U_i and V_{N-i+1} is ordered and the other is chaotic, which means that $\Phi(\lambda^i_{\max}) \neq \Phi(\Lambda^{N-i+1}_{\max})$, where $\Phi(X)$ is the Heaviside function. As shown in Fig. 3(d), there exist many blue curves that are completely achiral with the red curve. Therefore, the condition for $C = 1$ is stricter than that for $C = 0$. For general cases, $C \in (0, 1)$ and $S \in (0, 1)$ denote the average degree of chirality and symmetry between parameter-dependent evolution processes, respectively.

We apply the metrics S and C to describe the chirality and the symmetry between the chaotic dynamics in Figs. 2(a) and 2(b). As shown in Fig. 2(e), the φ-dependent chiral order-to-chaos transition processes (i.e., for given $|\xi|$, $\varphi \in [-\pi, \pi]$) show strong consistency with the value of C, i.e., $C = 1$. Moreover, the relation between the S curve and $|\xi|$ is consistent with the structural characteristics of the two phase diagrams. From Figs. 2(a) and 2(b), we find that when $|\xi|/\Omega \geq 3.4$ and $|\xi|/\Omega \leq 2.7$, the chaotic regimes in the phase diagrams are very narrow, and the distributions of the ordered regimes are relatively symmetrical on the φ axis. Therefore, the symmetry between the two parameter-dependent evolution processes on the φ axis is relatively high, as indicated by the value of S illustrated in Fig. 2(e). For $2.7 < |\xi|/\Omega < 3.4$, the chaotic regimes and the ordered regimes are intertwined on the φ axis, and thus the symmetry between two evolution processes decreases. The value of S is also small in this region, e.g., $S = 0.26$ for the representative point $|\xi|/\Omega = 3.1$. The $|\xi|$-dependent order-to-chaos transition processes (i.e., for given φ, $|\xi|/\Omega \in [2.5, 3.8]$) on the phase diagrams can also be accurately described by the S curve and the C curve. It is obvious that Figs. 2(a) and 2(b) show poor chirality along the $|\xi|$ axis. Therefore, for any given φ, $C < 1$, as illustrated in Fig. 2(f). Moreover, for the trivial gauge phase, i.e., $\varphi = \mathbb{Z}\pi$, where Z denotes any integer, the two parameter-dependent evolution processes along the $|\xi|$ axis are symmetrical (the system maintains time-reversal symmetry). The value of S also accurately reflects this phenomenon. As shown in Fig. 2(f), for the representative point $\varphi = 0$, $S = 1$.

IV. CHIRAL CHAOS FOR SENSING

We observe that the steplike rise or drop in Figs. 2(c) and 2(d) corresponds to the order-chaos phase transition, which can be verified via the power spectra of light fields in experiments [21,62–64]. As illustrated in the insets in Fig. 2(c) and the transition process $O \to M$ in Fig. 2(d), near the critical point, even a small perturbation $\delta\varphi$ may induce an abrupt change in the working state of the device, e.g., $\delta\varphi = \varphi_2 - \varphi_1 = 0.02\pi$ in Fig. 2(c). In the phase space, if the trajectories exhibit limit-cycle characteristics (i.e., discrete orbits), then the corresponding working states are ordered, e.g., $\varphi_2 = -0.18\pi$; if the trajectories are intertwined, forming a variety of solid ribbon structures in the phase space, then the corresponding working states are chaotic, e.g., $\varphi_1 = -0.2\pi$. Such phenomena have potential applications in high-precision sensing [30]. However, the orientation randomness of the perturbation $\delta\varphi$, i.e., positive deviation $\delta\varphi > 0$ (denoted by $+\delta\varphi$) and negative deviation $\delta\varphi < 0$ (denoted by $-\delta\varphi$) is random, and may result in false negative errors in conventional chaos-based sensing, as shown in the $O \to O'$ error in Fig. 2(d). These errors seriously limit the detection efficiency and success rate of conventional chaos-based sensing.

In our chiral chaotic device, the order-to-chaos transition processes or period-doubling bifurcation cascades no longer fully overlap for different pumping ports, as shown by the red and blue curves in Fig. 4(a). It is obvious that the two transition processes show chirality on the φ axis, and there is a certain distance between the corresponding two transition boundaries, e.g., the black-dashed boxes in Fig. 4(a). Therefore, we can construct a series of stable sensing windows. When the device works in the sensing window, the detection of a weak signal can be achieved by one splitting it into two signals, which are alternatively switched to the two ports. In this case, we find that the working state

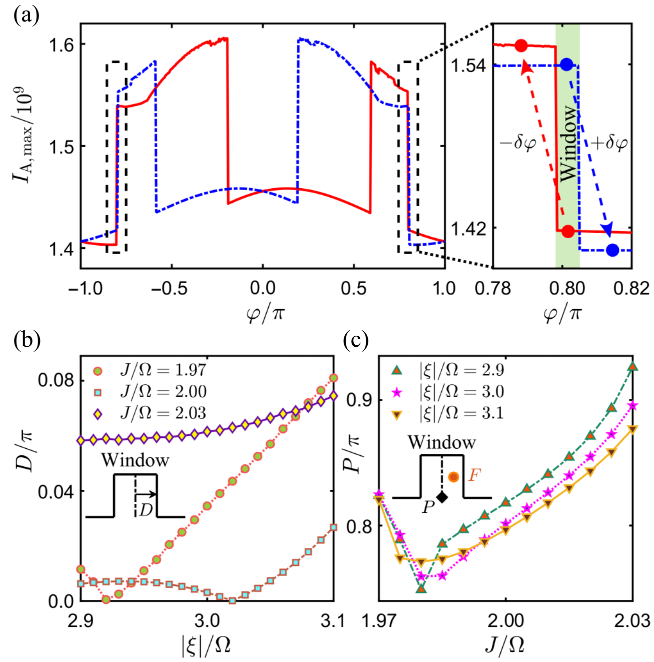

FIG. 4. (a) Maximum magnitude of the light intensity in resonator A (we define $I_{A,max} = \max\{|a_{CW}(\tau)|^2 + |a_{CCW}(\tau)|^2\}$) versus φ, where $|\xi|/\Omega = 3$. The red and blue curves represent the results of pumping from port 1 and port 2, respectively. Here, the properties of the right and left sensing windows within the black-dashed boxes are identical, and the right one is enlarged for the convenience of observation. The width of the windows is determined by the equivalent distance between two phase transition boundaries generated by pumping from port 1 and port 2, i.e., the width of the green strip. (b),(c) Tunability of the sensing window half-width D and center position P. F represents the working point of the device. Other parameters are the same as those in Fig. 2.

of the device is sensitive only to the strength (i.e., $|\delta\varphi|$) of the perturbation $\delta\varphi$, regardless of its deviation orientation.

The performance of the sensing window depends mainly on its half-width D, center position P, and working point F. Here we investigate the performance of the right sensing window in Fig. 4(a). The left and right sensing windows are chiral along the φ axis and share identical properties. The selection of F depends on the detection requirements and is independent of D and P. Moreover, as shown in Figs. 4(b) and 4(c), the values of D and P can be tuned via the parameters J, $|\xi|$, and φ. By the application of nanopositioning translation stages, various parameters of the device can be precisely controlled [44,65]. Therefore, the sensing windows in the device proposed have excellent tunability. By comparing the effects of $|\xi|$ and J on the windows in Figs. 4(b) and 4(c), we find that J plays a dominant role. This suggests that the variation of the distance between the two resonators is suitable as a coarse tuning method, while fiber tips are suitable as fine-tuning knobs. According to the expected detection accuracy and the value of D, we further divide the types of sensing windows and their application fields: (1) Narrow windows, with small D values, are suitable for sensitive sensing. The narrower the window, the higher the sensitivity that can be achieved. (2) Broad windows, with large D values, are suitable for threshold alarms [66,67]. The D value can be adjusted according to the specific threshold requirement. The equivalent distance between F and P is also an important parameter in determining the sensitivity of sensing windows, which can be regulated via tips, as shown in Fig. 4(c). In this paper, we concentrate on how to control the phase transition boundaries that construct the sensing window. Therefore, we discuss only the tunability of the center position P and the half-width D of the sensing windows, rather than the magnitude of changes in physical quantities, such as light intensity difference, before and after the phase transition.

The sensing windows on the φ axis can be generalized to other parameter planes. We now focus on the sensing windows constructed on the (ε, ω) plane, where ε and ω denote the amplitude and frequency of the pumping field. In Appendix E, we show that the half-width D and center position P of the sensing windows can be continuously tuned over a wide range. We assume that a detected signal with frequency $\omega + \delta\omega$ and amplitude $\delta\varepsilon$ ($\delta\varepsilon \ll \varepsilon$) is applied to the device via a tapered fiber. Therefore, the total input field becomes $E_{\rm tot} = \varepsilon_{\rm tot}\cos(\omega\tau + \theta_{\rm tot})$, in which

$$\begin{aligned} \varepsilon_{\rm tot} &= \sqrt{\varepsilon^2 + \delta\varepsilon^2 + 2\varepsilon\delta\varepsilon\cos(\delta\omega\tau + \theta)}, \\ \theta_{\rm tot} &= \arctan\left[\frac{\delta\varepsilon\sin(\delta\omega\tau + \theta)}{\varepsilon + \delta\varepsilon\cos(\delta\omega\tau + \theta)}\right]. \end{aligned} \tag{7}$$

$\varepsilon_{\rm tot}$ and $\theta_{\rm tot}$ are the equivalent amplitude and additional phase, where θ is the initial phase difference between the pumping field and the detected weak signal. More details are provided in Appendix E. To demonstrate the sensing performance, we now classify the sensing results into two categories, i.e., failure and success, on the basis of the following two criteria: (1) An order-to-chaos phase transition is induced. (2) The amplitudes of physical quantities (e.g., light intensities and mechanical oscillation amplitudes) are significantly changed. If both criteria are met after the weak detected signal is introduced, then we consider this a success; if both criteria are not met, we consider this a failure.

We take the detection of a monochromatic optical signal as an example to demonstrate the performance of the sensing windows. More complicated detected signals, e.g., signals with a certain bandwidth or background noise [7,68,69], will be discussed in follow-up work. We first consider the special case where the detected signal is in resonance with the pumping field, i.e., $\delta\omega = 0$, and the main results are shown in Figs. 5(a)–5(d). As illustrated in Fig. 5(a), for the conventional sensing proposal using the order-to-chaos phase transition [33], its effectiveness is strongly affected by the value of θ. Here, a large region of sensing failure (the yellow region) can be observed on the $(\delta\varepsilon, \theta)$ plane. However, θ cannot be known *a priori* in the actual sensing process, and is affected by various uncontrollable mechanisms [70,71]. This will inevitably lead to failure in some cases. Therefore, the corresponding success rate is low (the upper limit is 50%), as shown by the solid gray curve in Fig. 5(d). Compared with the conventional sensing principle, the chiral chaos–based sensing principle (for more details, see Appendix E) exhibits stronger robustness regarding θ. As shown in Fig. 5(b), for given φ, e.g., $\varphi/\pi = 0.505$, by one using a sensing window, the region of sensing success (the blue region) can be significantly expanded. The orange-dotted curve in Fig. 5(d) shows that the sensing success rate is increase by chiral chaos. If we optimize the selection of φ, i.e., tune the sensing window, the sensing success rate can approach 100%. For example, if $\varphi/\pi = 0.5$, as shown in Fig. 5(c) and the red-dashed curve in Fig. 5(d), the sensing success rate reaches 99.6%, which means that the false negative errors generated by the randomness of θ are suppressed effectively.

If $\delta\omega \neq 0$, the effective detectable range of $\delta\omega$, which is defined as the continuous range of $\delta\omega$ for sensing success, is an important indicator for evaluating the performance of sensing proposals [66]. Figure 5(e) shows a serious flaw of the conventional chaos-based sensing proposal, i.e., the effective detectable range is very narrow. We find that a series of sensing success regions show a striplike structure and are not connected to each other, which results in the effective detectable range, i.e., the blue region, being only a few megahertz. As illustrated in Fig. 5(f), the chiral chaos–based sensing proposal using a sensing window shows great advantages in this aspect. By the use of a sensing window, the striplike sensing success regions are connected to form large continuous regions. Therefore, a detectable range of tens of megahertz can be achieved. By one regulating the chiral chaos, i.e., optimizing the selection of φ, as shown in Fig. 5(g), the effective detectable range for $\varphi/\pi = 0.5$ can exceed 100 MHz. We emphasize that in practical applications the detectable range is also affected by the bandwidth of the pumping field. The sensing success rates in Fig. 5(h) also intuitively demonstrate the superiority of the chiral chaos–based sensing proposal. Our optimized sensing proposal (the red-dashed curve) consistently outperforms the conventional proposal (the solid gray curve). Moreover, our proposal allows the tuning of the chiral parameter φ to control the sensing windows (D and P), thereby optimizing sensing performance for specific scenarios. It is not easy to achieve such adaptability and tunability for the conventional chaos-based sensing proposal.

We further analyze these results. As shown in Eq. (7), if $\delta\omega = 0$, then θ controls the enhancement ($\varepsilon_{\rm tot} > \varepsilon$) or

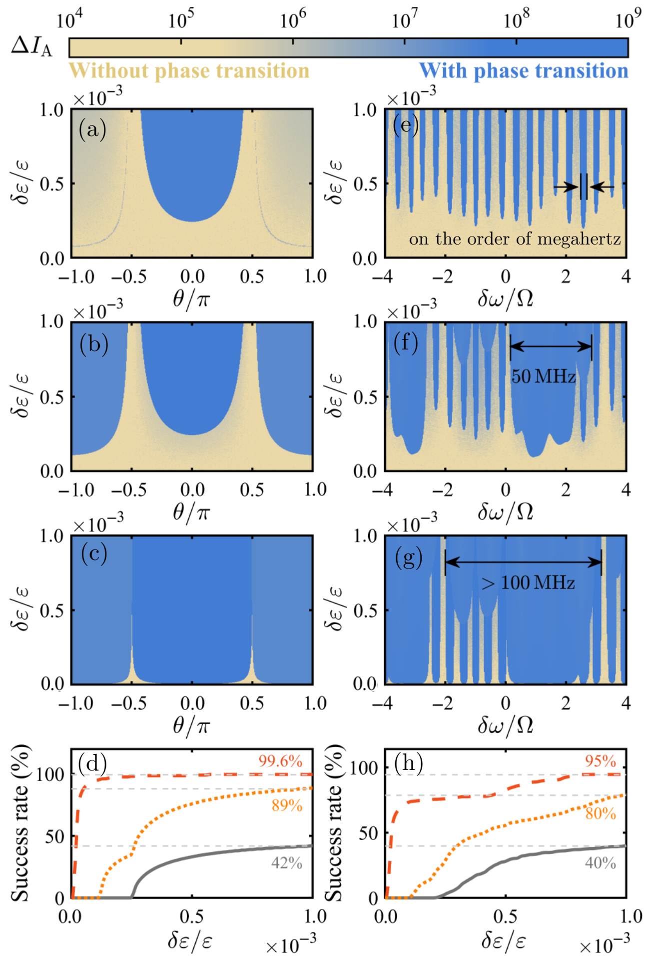

FIG. 5. (a),(e) Performance of the conventional chaos-based sensing proposal, which is obtained by one inputting the pumping field and weak detected signal from port 2. (b),(c),(f),(g) Performance of the chiral chaos–based sensing proposal using sensing windows. ΔI_A represents the change in the maximum light intensity in resonator A before and after the weak signal is introduced. Here, yellow and blue regions indicate sensing failure and success, respectively. We define the sensing success rate as the proportion of successful sensing events to the total events, for weak signals with given amplitude $\delta\varepsilon$. The sensing success rates from (a)–(c) and (e)–(g) are shown in (d),(h), respectively, in which solid gray, orange-dotted, and red-dashed curves correspond to (a),(e), to (b),(f), and to (c),(g), respectively. The parameters are as follows: (a)–(d) $\delta\omega = 0$, (e)–(h) $\theta/\pi = 0.5$ and $\Omega = 2\pi \times 20$ MHz, (a),(b),(e),(f) $\varphi/\pi = 0.505$, (c),(g) $\varphi/\pi = 0.5$. More details on the sensing windows can be found in Appendix E.

attenuation ($\varepsilon_{\rm tot} < \varepsilon$) of the pumping field. This implies that the upper limit of the success rate is only 50% for the conventional proposal, since the order-to-chaos transition can follow only one route (a specific direction), no matter how the detected signal is input. However, for the chiral chaos–based sensing proposal using sensing windows [see Fig. 4(a) or Fig. 9 in Appendix E], the situation changes dramatically. By the splitting of the signal into two signals, which are alternatively switched to the two ports, the order-to-chaos transition through a sensing window can proceed along two opposite directions. This means that the theoretical upper limit of the sensing success rate approaches 100%.

For $\delta\omega \neq 0$, θ affects mainly the initial conditions. The modulation of the pumping laser field by the weak signal is nonmonotonic, i.e., $\varepsilon_{\rm tot}$ and $\theta_{\rm tot}$ vary periodically, and the period is controlled by $\delta\omega$, as shown in Eq. (7). Thus, the working state of the device undergoes the chaos-order transition during half the time, while it holds the current state for the other half. The final effect induced by a weak signal depends on the structure of the chaotic attractors and initial conditions [37,72]. For chiral chaos, the structures of the attractors corresponding to the two pumping ports are inconsistent, resulting in more attractors gathered in the sensing window. Therefore, the effective detectable range of the chiral chaos–based sensing proposal is broader than that of the conventional chaos-based proposal.

V. DISCUSSION AND CONCLUSIONS

We propose and study chiral chaos via optomechanical systems. The chiral chaos phenomena are demonstrated through phase diagrams, bifurcation diagrams, Lyapunov exponents, etc. We develop metrics based on the Lyapunov exponents to quantitatively characterize the symmetry and chirality in chaotic dynamics.

By using the sensing windows constructed through chiral chaos, we show that the false negative errors plaguing conventional chaotic sensing can be effectively overcome. The controllable sensing windows in the parameter plane are applicable to different application scenarios, while maintaining the inherent advantages of nonlinear and chaos-based sensing. Moreover, under certain conditions, the effective detectable range of chaos-based sensing is also greatly broadened via the sensing windows. The proposed chiral chaotic device is sensitive to (1) the relative spatial distance between components, such as the distance between the resonators and the distance between the tips; (2) the polarizability of the tips, which is influenced by factors such as the material, size, and shape; and (3) the surrounding medium environment. Thus, the device may find applications in environmental quality monitoring and mechanical displacement sensing.

In current experiments, high-quality WGM resonators with mechanical modes already have a mature fabrication process [73,74]. The required quality factors are $Q_A = 4 \times 10^7$ for resonator A and $Q_B = 2 \times 10^6$ for resonator B. The diameters of both microtoroid resonators are in the range of 40–60 μm, with a mode volume of 200 $\mu{\rm m}^3$ for the optical modes. The tips are made of silica, and the tip surface can be electroplated with various materials, such as chromium, to increase the regulation ability of the tips

[42]. These specifications are achievable with current fabrication technologies [75–78]. Moreover, the optomechanical interactions via radiation pressure in resonator A can be tuned by secondary etching [79]. The coupling parameters between optical modes can be precisely regulated with the use of nanopositioning translation stages and fiber tips [65,80]. Thus, our proposal is feasible under current experimental conditions for optomechanical systems. With the rapid progress of the study of quantum information processing, many physical systems are being developed to have radiation-pressure-type nonlinear interactions. For example, in superconducting quantum circuits, radiation-pressure-type nonlinear interactions between microwave fields and mechanical resonators can be realized [81,82]. Surface acoustic waves [83] can also be coupled to other mechanical vibrations via radiation-pressure-type interaction [84]. Thus, our proposal may also be applied to these physical systems.

ACKNOWLEDGMENTS

Y.L. is supported by the National Natural Science Foundation of China (Grants No. 12374483 and No. 92365209). J.Z. is supported by the Laoshan Laboratory (Grant No. LSKJ202200900); the Leading Scholar of Xi'an Jiaotong University; innovative leading talent project of Shuangqian plan in Jiangxi Province.

APPENDIX A: DETAILS ON THE CHIRAL CHAOTIC DEVICE

1. Tip-induced coupling between optical modes

The electric field distribution in resonator B is given by

$$\hat{\mathbf{E}}(\mathbf{r},t) = \mathbf{E}(\mathbf{r})e^{-i\omega_{\mathrm{B}}t}(\hat{b}_{\mathrm{CW}}e^{i\mathbf{k}\cdot\mathbf{r}} + \hat{b}_{\mathrm{CCW}}e^{-i\mathbf{k}\cdot\mathbf{r}} + \mathrm{H.c.}),$$
$$\mathbf{E}(\mathbf{r}) = \sqrt{\frac{\hbar\omega_{\mathrm{B}}}{2\varepsilon_0 V_{\mathrm{B}}}} f(\mathbf{r})\hat{\mathbf{e}}(\mathbf{r}), \tag{A1}$$

where ω_{B} and V_{B} represent the resonance frequency and quantization volume of WGMs in resonator B, ε_0 denotes the vacuum permittivity, $\hat{b}_{\mathrm{CW}}$ and $\hat{b}^{\dagger}_{\mathrm{CW}}$ ($\hat{b}_{\mathrm{CCW}}$ and $\hat{b}^{\dagger}_{\mathrm{CCW}}$) denote the annihilation and creation operators for the CW mode (CCW mode) in resonator B, $\mathbf{k}$ ($-\mathbf{k}$) represents the wave vector of the CW mode (CCW mode), and $\hat{\mathbf{e}}(\mathbf{r})$ and $f(\mathbf{r})$ denote the unit vector of the electric field direction and the cavity-mode function at position $\mathbf{r}$. The two fiber tips contact the rim of resonator B at $\mathbf{r}_1$ and $\mathbf{r}_2$, causing them to be polarized by the evanescent fields, which can be described as

$$\hat{\mathbf{P}}(\mathbf{r}_1,t) = \varepsilon_0\chi_1\hat{\mathbf{E}}(\mathbf{r}_1,t), \quad \hat{\mathbf{P}}(\mathbf{r}_2,t) = \varepsilon_0\chi_2\hat{\mathbf{E}}(\mathbf{r}_2,t), \tag{A2}$$

where χ_1 and χ_2 represent the polarizability of tip 1 and tip 2, respectively. By using the dipole approximation and the rotating-wave approximation, and considering the backscattering processes with strength ξ_0 induced by surface defects, we can write the interaction energy between CW and CCW modes as

$$\begin{aligned}\hat{V} &= -\frac{1}{2}\hat{\mathbf{P}}(\mathbf{r}_1,t)\cdot\hat{\mathbf{E}}(\mathbf{r}_1,t) - \frac{1}{2}\hat{\mathbf{P}}(\mathbf{r}_2,t)\cdot\hat{\mathbf{E}}(\mathbf{r}_2,t) + \hat{V}_0\\ &= -\hbar|\xi|(e^{i\varphi}\hat{b}^{\dagger}_{\mathrm{CW}}\hat{b}_{\mathrm{CCW}} + e^{-i\varphi}\hat{b}_{\mathrm{CW}}\hat{b}^{\dagger}_{\mathrm{CCW}})\\ &\quad - \hbar\delta(\hat{b}^{\dagger}_{\mathrm{CW}}\hat{b}_{\mathrm{CW}} + \hat{b}^{\dagger}_{\mathrm{CCW}}\hat{b}_{\mathrm{CCW}}),\end{aligned} \tag{A3}$$

in which

$$\begin{aligned}|\xi|e^{\pm i\varphi} &= \xi_0 + \frac{\omega_{\mathrm{B}}\left[\chi_1 f^2(\mathbf{r}_1) + \chi_2 f^2(\mathbf{r}_2)e^{\pm i2n\beta}\right]}{2V_{\mathrm{B}}},\\ \hat{V}_0 &= -\hbar\xi_0(\hat{b}^{\dagger}_{\mathrm{CW}}\hat{b}_{\mathrm{CCW}} + \hat{b}_{\mathrm{CW}}\hat{b}^{\dagger}_{\mathrm{CCW}}),\\ \delta &= \frac{\omega_{\mathrm{B}}\left[\chi_1 f^2(\mathbf{r}_1) + \chi_2 f^2(\mathbf{r}_2)\right]}{2V_{\mathrm{B}}}.\end{aligned} \tag{A4}$$

Note that the dipole-dipole interaction has been ignored due to the sufficient distance between the fiber tips. Without loss of generality, we assume that $\mathbf{r}_1$ is the coordinate origin. n is the azimuthal order corresponding to the wave vector $\mathbf{k}$, i.e., the number of wavelengths in the perimeter of resonator B, δ is the frequency shift of the optical modes induced by the two tips, and β is the spatial phase difference between the two tips. According to the current experimental conditions [65,75], as illustrated in Fig. 6(a), we calculate the achievable range of δ.

2. Tip-induced broadening on optical modes

Besides inducing couplings between optical modes, the two tips also result in additional linewidth broadening on the optical modes. The Hamiltonian of the optical modes coupled to the reservoir modes can be expressed as

$$\begin{aligned}\hat{H} &= \hbar\omega_{\mathrm{B}}(\hat{b}^{\dagger}_{\mathrm{CW}}\hat{b}_{\mathrm{CW}} + \hat{b}^{\dagger}_{\mathrm{CCW}}\hat{b}_{\mathrm{CCW}}) + \sum_s \hbar\omega_s\hat{c}^{\dagger}_s\hat{c}_s\\ &\quad - \sum_{l,s}\hbar g_{l,s}\left[\hat{b}^{\dagger}_{\mathrm{CW}}\hat{c}_s e^{i(\mathbf{k}_s-\mathbf{k})\cdot\mathbf{r}_l} + \hat{b}^{\dagger}_{\mathrm{CCW}}\hat{c}_s e^{i(\mathbf{k}_s+\mathbf{k})\cdot\mathbf{r}_l} + \mathrm{H.}c.\right],\end{aligned} \tag{A5}$$

where $\hat{c}_s$ and $\hat{c}^{\dagger}_s$ denote the annihilation and creation operators of the sth reservoir mode with frequency ω_s, respectively, and $g_{l,s} = \chi_l f(\mathbf{r}_l)\sqrt{\omega_{\mathrm{B}}\omega_s/4V_{\mathrm{B}}V_{\mathrm{vac}}}\,\hat{\mathbf{e}}_l\cdot\hat{\mathbf{e}}_s$ represents the coupling strength between the optical modes and the sth reservoir mode induced by tip l positioned at $\mathbf{r}_l$, where $\hat{\mathbf{e}}_s$ and V_{vac} denote the unit vector and the quantization volume of the sth reservoir mode, and $\hat{\mathbf{e}}_l$ denotes the unit vector of WGMs. Then the Heisenberg-Langevin

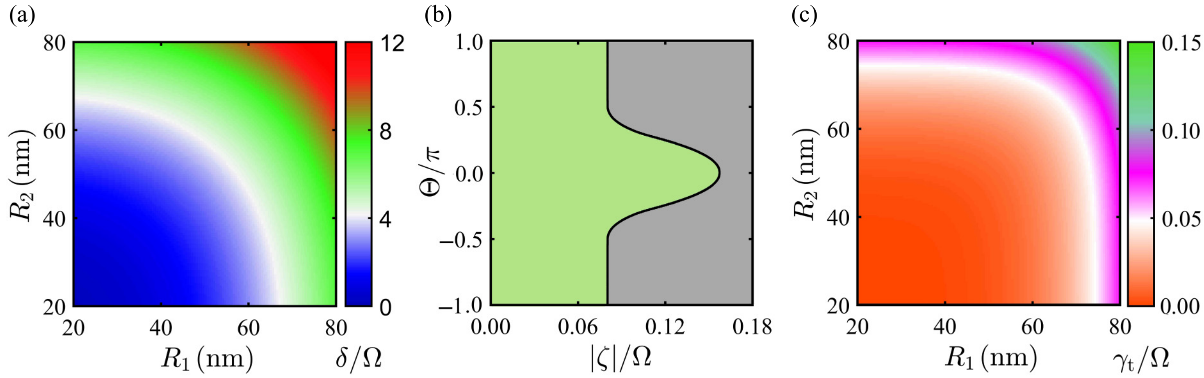

FIG. 6. (a) δ as a function of the geometric scale (effective radius) of the two tips. (b) $|\zeta|e^{\pm i\Theta}$ as a function of the geometric scale (effective radius) and relative position of the two tips, where the green and gray regions represent the achievable and unachievable ranges. (c) γ_t as a function of the geometric scale (effective radius) of the two tips. The following parameters are used in all the figures: $n_1^2 = 3.9$, $n_2^2 = 3.9$, $\Omega = 2\pi \times 20$ MHz, $f(\mathbf{r}_1) = f(\mathbf{r}_2) = 0.3$, $V_B = 200\ \mu\mathrm{m}^3$, $v = 3 \times 10^8$ m/s, $\omega_B = 2\pi \times 193$ THz, $\beta \in [-\pi, \pi]$, $R_1 \in [20, 80]$ nm, and $R_2 \in [20, 80]$ nm.

equations can be obtained as

$$\dot{\hat{b}}_{\mathrm{CW}} = -i\omega_B \hat{b}_{\mathrm{CW}} + i\sum_{l,s} g_{l,s}\hat{c}_s e^{i(\mathbf{k}_s-\mathbf{k})\cdot\mathbf{r}_l}, \tag{A6}$$

$$\dot{\hat{b}}_{\mathrm{CCW}} = -i\omega_B \hat{b}_{\mathrm{CCW}} + i\sum_{l,s} g_{l,s}\hat{c}_s e^{i(\mathbf{k}_s+\mathbf{k})\cdot\mathbf{r}_l}, \tag{A7}$$

$$\dot{\hat{c}}_s = -i\omega_s \hat{c}_s + i\sum_{l} g_{l,s}\left[\hat{b}_{\mathrm{CW}} e^{-i(\mathbf{k}_s-\mathbf{k})\cdot\mathbf{r}_l} + \hat{b}_{\mathrm{CCW}} e^{-i(\mathbf{k}_s+\mathbf{k})\cdot\mathbf{r}_l}\right]. \tag{A8}$$

Further processing Eq. (A8) through formal integration, we obtain

$$\hat{c}_s(t) = \hat{c}_s(0)e^{-i\omega_s t} + i\sum_{l} g_{l,s}\int_0^t \left[\hat{b}_{\mathrm{CW}}(t')e^{-i(\mathbf{k}_s-\mathbf{k})\cdot\mathbf{r}_l} + \hat{b}_{\mathrm{CCW}}(t')e^{-i(\mathbf{k}_s+\mathbf{k})\cdot\mathbf{r}_l}\right] e^{-i\omega_s(t-t')}dt'. \tag{A9}$$

To simplify the following discussion, we now separate the slowly varying and rapidly oscillating contributions of the CW and CCW modes

$$\hat{b}_{\mathrm{CW}}(t) = \tilde{b}_{\mathrm{CW}}(t)e^{-i\omega_B t}, \quad \hat{b}_{\mathrm{CCW}}(t) = \tilde{b}_{\mathrm{CCW}}(t)e^{-i\omega_B t}. \tag{A10}$$

Substituting Eqs. (A9) and (A10) into Eqs. (A6) and (A7), we can rewrite Eqs. (A6) and (A7) as

$$\dot{\tilde{b}}_{\mathrm{CW}}(t) = -\sum_{l,s} g_{l,s}^2 \int_0^t \left[\tilde{b}_{\mathrm{CW}}(t') + \tilde{b}_{\mathrm{CCW}}(t')e^{-i2\mathbf{k}\cdot\mathbf{r}_l}\right] e^{-i(\omega_s-\omega_B)(t-t')}dt' + i\sum_{l,s} g_{l,s}\hat{c}_s(0)e^{-i(\omega_s-\omega_B)t}e^{i(\mathbf{k}_s-\mathbf{k})\cdot\mathbf{r}_l}, \tag{A11}$$

$$\dot{\tilde{b}}_{\mathrm{CCW}}(t) = -\sum_{l,s} g_{l,s}^2 \int_0^t \left[\tilde{b}_{\mathrm{CCW}}(t') + \tilde{b}_{\mathrm{CW}}(t')e^{i2\mathbf{k}\cdot\mathbf{r}_l}\right] e^{-i(\omega_s-\omega_B)(t-t')}dt' + i\sum_{l,s} g_{l,s}\hat{c}_s(0)e^{-i(\omega_s-\omega_B)t}e^{i(\mathbf{k}_s+\mathbf{k})\cdot\mathbf{r}_l}, \tag{A12}$$

where the coupling terms between the CW and CCW modes at different positions induced by the reservoir have been ignored. The fluctuation operators associated with $\hat{c}_s(0)$ are ignored in the following, since they have no effect on the mean-value equations ($\langle\hat{c}_s(0)\rangle = 0$). If we assume that the reservoir modes are closely spaced in frequency, then the following substitution relation holds:

$$\sum_s \to \frac{2V_{\mathrm{vac}}}{(2\pi v)^3}\int_0^{2\pi} d\phi \int_0^{\pi} \sin(\theta)d\theta \int_0^{\infty} \omega_s^2 d\omega_s, \tag{A13}$$

where we have set the optical fields to be polarized along the z axis, θ and ϕ describe the polarization direction of the reservoir field in the spherical coordinate system, and v is the velocity of light in the medium surrounding resonator B. Combining Eqs. (A11)–(A13), we get the tip-induced broadening on the CW and CCW modes as

$$\begin{aligned}\dot{\tilde{b}}_{\rm CW}(t) &= -\gamma_{\rm t}\tilde{b}_{\rm CW}(t) - |\zeta|e^{i\Theta}\tilde{b}_{\rm CCW}(t),\\ \dot{\tilde{b}}_{\rm CCW}(t) &= -\gamma_{\rm t}\tilde{b}_{\rm CCW}(t) - |\zeta|e^{-i\Theta}\tilde{b}_{\rm CW}(t),\end{aligned} \tag{A14}$$

in which

$$\begin{aligned}\gamma_{\rm t} &= \frac{\omega_{\rm B}^4\left[\chi_1^2 f^2(\mathbf{r}_1) + \chi_2^2 f^2(\mathbf{r}_2)\right]}{12\pi v^3 V_{\rm B}},\\ |\zeta|e^{\pm i\Theta} &= \frac{\omega_{\rm B}^4\left[\chi_1^2 f^2(\mathbf{r}_1) + \chi_2^2 f^2(\mathbf{r}_2)e^{\pm i2n\beta}\right]}{12\pi v^3 V_{\rm B}}.\end{aligned} \tag{A15}$$

If we further ignore the shape details of the tips and treat them as spheres, then the polarizability χ of the tips can be expressed as $\chi_l = 4\pi R_l^3(n_l^2-1)/(n_l^2+2)$, in which R_l and n_l denote the effective radius and the refractive index of the sphere scatterer, which is used to simulate the tip l. With the use of specific parameters, we calculate the achievable ranges of $|\zeta|e^{\pm i\Theta}$ and $\gamma_{\rm t}$, as shown in the green regions in Figs. 6(b) and 6(c). Moreover, Eqs. (A4) and (A15) state that δ and $|\xi|e^{\pm i\varphi}$ are proportional to R_l^3, but $\gamma_{\rm t}$ and $|\zeta|e^{\pm i\Theta}$ are proportional to R_l^6. Therefore, for the small-scale tip, i.e., $R_l \ll \lambda_{\rm B}$, where $\lambda_{\rm B}$ denotes the resonance wavelength of resonator B, $\{|\xi|e^{\pm i\varphi}, \delta\} \gg \{|\zeta|e^{\pm i\Theta}, \gamma_{\rm t}\}$, as illustrated in Figs. 6 and 1(c).

APPENDIX B: DETAILS ON CHIRAL CHAOTIC DYNAMICS

In experiments, the working states of the device can be detected by the temporal evolution, power spectrum, and phase-space trajectories of the intracavity light field [21]. Therefore, we present them all in Fig. 7. For pumping from port 1, as illustrated in Figs. 7(a), 7(e), and 7(i), $I_{\rm A}$ exhibits significant irregularities in the time domain, and its motion trajectories are intertwined, forming a variety of solid ribbon structures in the phase space. Moreover, the frequency spectrum of $I_{\rm A}$ appears continuous. These phenomena indicate that the proposed device is working in a chaotic state, which means that even if the equations of motion are deterministic, we cannot accurately predict the future working state of the device.

However, if we switch the pumping port from port 1 to port 2 and keep other the conditions unchanged, the working state of the device will change dramatically. As shown in Figs. 7(b) and 7(j), $I_{\rm A}$ shows the characteristics

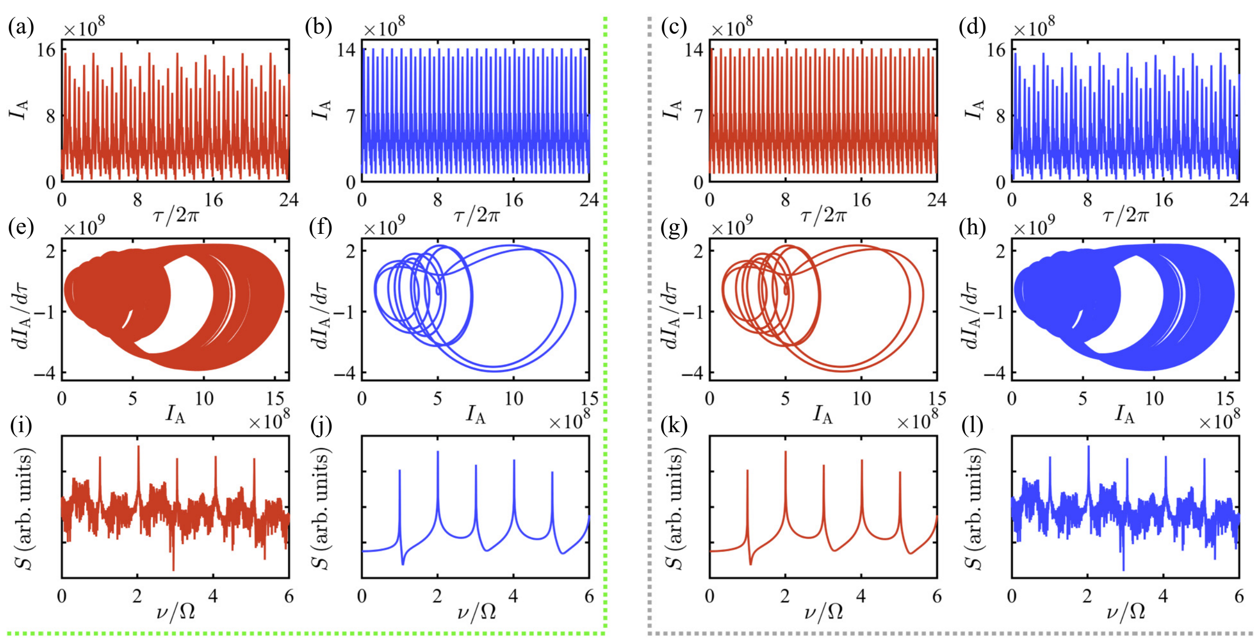

FIG. 7. (a)–(d) Time-domain evolution of the total light intensity $I_{\rm A}$ in resonator A (here $I_{\rm A} = |a_{\rm CW}|^2 + |a_{\rm CCW}|^2$) for pumping from port 1 (red) and port 2 (blue), under different parameter conditions. The scattering phases in the two regions demarcated by the green-dotted and gray-dotted curves are $\varphi/\pi = 0.755$ and $\varphi/\pi = -0.755$, respectively. (e)–(h) Corresponding phase-space trajectories. (i)–(l) Corresponding frequency spectra. Considering the current fabrication techniques for WGM resonators [19,22], the other parameters chosen here are $\Omega = 2\pi \times 20$ MHz, $G/\Omega = 5\times 10^{-5}$, $\Gamma/\Omega = 5\times 10^{-3}$, $\Delta_{\rm A}/\Omega = -0.5$, $\Delta_{\rm B}/\Omega = -0.5$, $\eta/\Omega = 0.15$, $J/\Omega = 2$, $|\xi|/\Omega = 3.29$, $\kappa/\Omega = 0.25$, $\gamma/\Omega = 5$, and $\varepsilon/\Omega = 5.8\times 10^4$.

of periodic oscillations, which can be observed more intuitively from the frequency spectrum. Obviously, discrete peaks occur only at integer multiples of Ω. Although the trajectories in the phase space appear somewhat disorganized, the limit-cycle characteristics can still be discerned, as illustrated in Fig. 7(f). These phenomena indicate that the device is working in an ordered state. In summary, the Lorentz reciprocity of the device has been broken (except for some special cases, which are discussed in detail later), and the same conclusion can be drawn from Figs. 7(c), 7(d), 7(g), 7(h), 7(k), and 7(l).

Another important finding is that if the hopping phase is transformed from φ to $-\varphi$ after switching of the working port, then the dynamics of the device remain unchanged [compare Figs. 7(a), 7(b), 7(e), 7(f), 7(i), and 7(j) with Figs. 7(c), 7(d), 7(g), 7(h), 7(k), and 7(l)]. To show this phenomenon more intuitively, we present the bifurcation diagrams of the mechanical oscillation amplitude (versus φ) under two pumping conditions in Figs. 8(a) and 8(b). Here, we count the number of bifurcations to distinguish different working states [17,20]. More specifically, in the bifurcation diagram, one point, multiple points, and infinite points represent the self-induced oscillation, period-doubling bifurcations, and chaotic states, respectively. A noteworthy phenomenon is that no matter which port is pumped, the device can be switched between regular and chaotic states by one changing the parameter φ. However, such switching processes are not completely independent for different pumping ports. From comparison of the diagrams in Figs. 8(a) and 8(b), it can be intuitively found that they satisfy chiral symmetry on the φ-axis, which is even more evident in the two insets. Thus, we conclude that the device supports a chiral chaotic working state.

Moreover, it is worth noting that in certain parameter regions, the chaotic states can appear only in one specific pumping direction. To more intuitively demonstrate this nonreciprocal chaotic state, we present the representative results in Figs. 8(c) and 8(d), which demonstrate that the response of the device to external pumping with frequency ω and amplitude ε also depends on the pumping port. As illustrated in the red parts in Figs. 8(c) and 8(d), for pumping from the port 1, tuning of ω and ε can control the device to operate in the desired regime, either chaotic or regular. However, after switching of the pumping port, as illustrated in the blue parts in Figs. 8(c) and 8(d), the device is restricted to working in the regular regime, which means that all chaotic phenomena are unavailable. Similar nonreciprocal behaviors exist in other parameter regions. Therefore, the chiral chaotic device designed can be applied to realize multiple types of nonreciprocal signal modulation, which indicates its potential applications in communication networks and information processing.

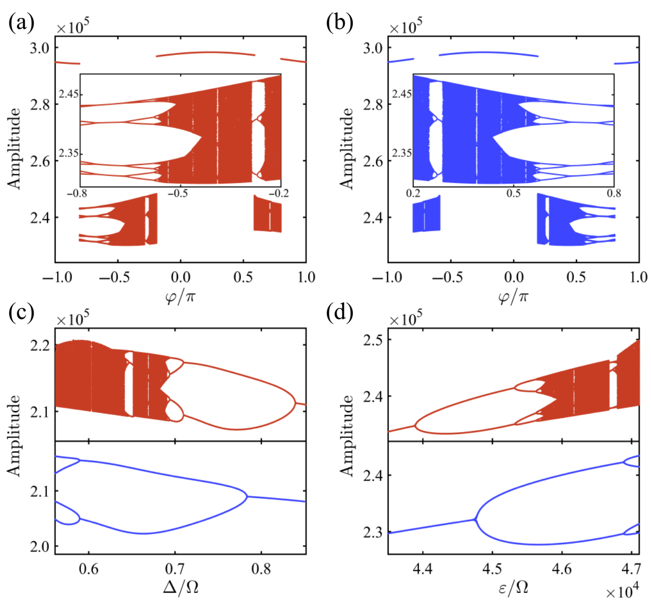

FIG. 8. Bifurcation diagrams of the mechanical oscillation amplitude for pumping from port 1 (red) and port 2 (blue), under different parameter conditions. For (a), (b), $|\xi|/\Omega = 3$, and the insets show enlarged views; for (c), $\Delta = \omega_A - \omega = \omega_B - \omega$, $\varepsilon/\Omega = 5.4 \times 10^4$, $|\xi|/\Omega = 5$, and $\varphi/\pi = 0.5$; for (d), $\varphi/\pi = 0.5$ and $|\xi|/\Omega = 10$; the other parameters are the same as in Fig. 7.

APPENDIX C: DETAILS ON GAUGE TRANSFORMATION AND TIME-REVERSAL SYMMETRY

Physically, the chirality in chaotic dynamics originates from the regulation of time-reversal symmetry of CW and CCW modes by the two fiber tips. We now demonstrate this from the perspective of gauge transformation. According to the standard analysis method, if the device maintains time-reversal symmetry, the Hamiltonian $\hat{H}$ satisfies the following transformation relation: $\hat{\Theta}\hat{H}\hat{\Theta}^{-1} = \hat{H}$, where $\hat{\Theta}$ is the antiunitary and antilinear time-reversal operation. Moreover, the transformation relations for the optical and mechanical operators under time reversal read

$$\hat{\Theta}\hat{a}_{\mathrm{CW}}\hat{\Theta}^{-1} = e^{i\theta_1}\hat{a}_{\mathrm{CW}}, \quad \hat{\Theta}\hat{a}_{\mathrm{CCW}}\hat{\Theta}^{-1} = e^{i\theta_2}\hat{a}_{\mathrm{CCW}}, \quad \text{(C1)}$$

$$\hat{\Theta}\hat{b}_{\mathrm{CW}}\hat{\Theta}^{-1} = e^{i\theta_3}\hat{b}_{\mathrm{CW}}, \quad \hat{\Theta}\hat{b}_{\mathrm{CCW}}\hat{\Theta}^{-1} = e^{i\theta_4}\hat{b}_{\mathrm{CCW}}, \quad \text{(C2)}$$

$$\hat{\Theta}\hat{p}\hat{\Theta}^{-1} = -\hat{p} + \nabla\vartheta, \quad \hat{\Theta}\hat{q}\hat{\Theta}^{-1} = \hat{q}, \quad \text{(C3)}$$

in which θ_1, θ_2, θ_3, θ_4, and ϑ denote the linear gauge phases. One can easily verify that, by using the gauge phases, the following relations are always satisfied:

$$\hat{\Theta}(\hat{a}^\dagger_{\rm CW}\hat{a}_{\rm CW}+\hat{a}^\dagger_{\rm CCW}\hat{a}_{\rm CCW})\hat{q}\hat{\Theta}^{-1}=(\hat{a}^\dagger_{\rm CW}\hat{a}_{\rm CW}+\hat{a}^\dagger_{\rm CCW}\hat{a}_{\rm CCW})\hat{q}, \tag{C4}$$

$$\hat{\Theta}(\hat{a}^\dagger_{\rm CW}\hat{a}_{\rm CW}+\hat{a}^\dagger_{\rm CCW}\hat{a}_{\rm CCW})\hat{\Theta}^{-1}=\hat{a}^\dagger_{\rm CW}\hat{a}_{\rm CW}+\hat{a}^\dagger_{\rm CCW}\hat{a}_{\rm CCW}, \tag{C5}$$

$$\hat{\Theta}(\hat{b}^\dagger_{\rm CW}\hat{b}_{\rm CW}+\hat{b}^\dagger_{\rm CCW}\hat{b}_{\rm CCW})\hat{\Theta}^{-1}=\hat{b}^\dagger_{\rm CW}\hat{b}_{\rm CW}+\hat{b}^\dagger_{\rm CCW}\hat{b}_{\rm CCW}, \tag{C6}$$

$$\hat{\Theta}(\hat{p}^2+\hat{q}^2)\hat{\Theta}^{-1}=\hat{p}^2+\hat{q}^2 \quad \text{for } \nabla\vartheta(\hat{q})=0. \tag{C7}$$

However, this is not the case for interactions between the optical modes. According to Eqs. (C1) and (C2), we can obtain the following transformation relations:

$$\hat{\Theta}(\hat{a}^\dagger_{\rm CW}\hat{b}_{\rm CCW}+\hat{a}_{\rm CW}\hat{b}^\dagger_{\rm CCW})\hat{\Theta}^{-1}=e^{i(\theta_4-\theta_1)}\hat{a}^\dagger_{\rm CW}\hat{b}_{\rm CCW}+e^{i(\theta_1-\theta_4)}\hat{a}_{\rm CW}\hat{b}^\dagger_{\rm CCW}, \tag{C8}$$

$$\hat{\Theta}(\hat{a}^\dagger_{\rm CCW}\hat{b}_{\rm CW}+\hat{a}_{\rm CCW}\hat{b}^\dagger_{\rm CW})\hat{\Theta}^{-1}=e^{i(\theta_3-\theta_2)}\hat{a}^\dagger_{\rm CCW}\hat{b}_{\rm CW}+e^{i(\theta_2-\theta_3)}\hat{a}_{\rm CCW}\hat{b}^\dagger_{\rm CW}, \tag{C9}$$

$$\hat{\Theta}(\hat{a}^\dagger_{\rm CW}\hat{a}_{\rm CCW}+\hat{a}_{\rm CW}\hat{a}^\dagger_{\rm CCW})\hat{\Theta}^{-1}=e^{i(\theta_2-\theta_1)}\hat{a}^\dagger_{\rm CW}\hat{a}_{\rm CCW}+e^{i(\theta_1-\theta_2)}\hat{a}_{\rm CW}\hat{a}^\dagger_{\rm CCW}, \tag{C10}$$

$$\hat{\Theta}(e^{i\varphi}\hat{b}^\dagger_{\rm CW}\hat{b}_{\rm CCW}+e^{-i\varphi}\hat{b}_{\rm CW}\hat{b}^\dagger_{\rm CCW})\hat{\Theta}^{-1}=e^{i(\theta_4-\theta_3-\varphi)}\hat{b}^\dagger_{\rm CW}\hat{b}_{\rm CCW}+e^{i(\theta_3-\theta_4+\varphi)}\hat{b}_{\rm CW}\hat{b}^\dagger_{\rm CCW}. \tag{C11}$$

Therefore, the gauge phases required for the Hamiltonian to satisfy the time-reversal transformation relation must meet the following conditions:

$$\begin{aligned}&\theta_4-\theta_1=2\pi\mathbb{Z}_1, \quad \theta_3-\theta_2=2\pi\mathbb{Z}_2,\\ &\theta_2-\theta_1=2\pi\mathbb{Z}_3, \quad \theta_3-\theta_4+2\varphi=2\pi\mathbb{Z}_4,\end{aligned} \tag{C12}$$

where $\mathbb{Z}_1$, $\mathbb{Z}_2$, $\mathbb{Z}_3$, and $\mathbb{Z}_4$ denote arbitrary integers. Further processing Eq. (C12), we can obtain the condition for the system to maintain time-reversal symmetry, i.e., $\varphi=\pi\mathbb{Z}$, where $\mathbb{Z}$ denotes an arbitrary integer. This indicates that the net hopping phase φ acquired by photons during the tip-induced backscattering processes can also be applied to control the working states of the chiral chaotic device. For nontrivial φ, i.e., $\varphi\neq\pi\mathbb{Z}$, as illustrated in Eqs. (C8)–(C11), its value is opposite for the two reverse loops. The value of φ for the loop $\hat{a}_{\rm CCW}\to\hat{b}_{\rm CW}\to\hat{b}_{\rm CCW}\to\hat{a}_{\rm CW}\to\hat{a}_{\rm CCW}$ is exactly the opposite of that for the reverse loop $\hat{a}_{\rm CCW}\to\hat{a}_{\rm CW}\to\hat{b}_{\rm CCW}\to\hat{b}_{\rm CW}\to\hat{a}_{\rm CCW}$, as illustrated in Fig. 1(b). This is the underlying reason for the chirality of the two chaotic dynamics of the device corresponding to the two opposite pumping directions on the φ axis.

APPENDIX D: DETAILS ON THE STEADY-STATE LIGHT INTENSITY DISTRIBUTIONS

Although the analytical expressions for chiral chaos are unavailable, we can analytically obtain the light intensity distributions under the steady-state condition, which also reveal the origin of chirality. For the steady state, Eqs. (2a)–(2e) can be rewritten as

$$0=(-i\Delta_{\rm A}^q-\kappa)a^{\rm s}_{\rm CW}+i\eta a^{\rm s}_{\rm CCW}+iJb^{\rm s}_{\rm CCW}+\varepsilon_1, \tag{D1}$$

$$0=(-i\Delta_{\rm A}^q-\kappa)a^{\rm s}_{\rm CCW}+i\eta a^{\rm s}_{\rm CW}+iJb^{\rm s}_{\rm CW}+\varepsilon_2, \tag{D2}$$

$$0=(-i\Delta_{\rm B}-\gamma)b^{\rm s}_{\rm CW}+i|\xi|e^{i\varphi}b^{\rm s}_{\rm CCW}+iJa^{\rm s}_{\rm CCW}, \tag{D3}$$

$$0=(-i\Delta_{\rm B}-\gamma)b^{\rm s}_{\rm CCW}+i|\xi|e^{-i\varphi}b^{\rm s}_{\rm CW}+iJa^{\rm s}_{\rm CW}, \tag{D4}$$

$$0=-\Omega q_{\rm s}+G(|a^{\rm s}_{\rm CW}|^2+|a^{\rm s}_{\rm CCW}|^2), \quad p_{\rm s}=0. \tag{D5}$$

Solving the above equations, we get the following results:

$$a^{\rm s}_{\rm CW}=-i\frac{\varepsilon_2(\eta+Fe^{-i\varphi})+\varepsilon_1\widetilde{\Delta}_{\rm A}}{\widetilde{\Delta}_{\rm A}^2-(\eta+Fe^{-i\varphi})(\eta+Fe^{i\varphi})}, \tag{D6}$$

$$a^{\rm s}_{\rm CCW}=-i\frac{\varepsilon_1(\eta+Fe^{i\varphi})+\varepsilon_2\widetilde{\Delta}_{\rm A}}{\widetilde{\Delta}_{\rm A}^2-(\eta+Fe^{-i\varphi})(\eta+Fe^{i\varphi})}, \tag{D7}$$

$$b^{\rm s}_{\rm CW}=\frac{J|\xi|e^{i\varphi}a^{\rm s}_{\rm CW}+J(\Delta_{\rm B}-i\gamma)a^{\rm s}_{\rm CCW}}{(\Delta_{\rm B}-i\gamma)^2-|\xi|^2}, \tag{D8}$$

$$b^{\rm s}_{\rm CCW}=\frac{J|\xi|e^{-i\varphi}a^{\rm s}_{\rm CCW}+J(\Delta_{\rm B}-i\gamma)a^{\rm s}_{\rm CW}}{(\Delta_{\rm B}-i\gamma)^2-|\xi|^2}, \tag{D9}$$

$$p_{\rm s}=0, \quad q_{\rm s}=\frac{G}{\Omega}(|a^{\rm s}_{\rm CW}|^2+|a^{\rm s}_{\rm CCW}|^2), \tag{D10}$$

in which

$$\begin{aligned}\widetilde{\Delta}_{\rm A}&=\Delta_{\rm A}-\frac{G^2}{\Omega}(|a^{\rm s}_{\rm CW}|^2+|a^{\rm s}_{\rm CCW}|^2)-i\kappa-\frac{F(\Delta_{\rm B}-i\gamma)}{|\xi|},\\ F&=\frac{J^2|\xi|}{(\Delta_{\rm B}-i\gamma)^2-|\xi|^2}.\end{aligned} \tag{D11}$$

Thus, the steady-state light intensities in resonator A $I^{\rm s}_{\rm A}$ ($I^{\rm s}_{\rm A}=|a^{\rm s}_{\rm CW}|^2+|a^{\rm s}_{\rm CCW}|^2$) corresponding to pumping from port 1 and port 2 can be expressed as

$$I^{s}_{A,1} = g(|\widetilde{\Delta}_A|^2 + |\eta + Fe^{i\varphi}|^2), \quad \text{pumping from port 1,}$$
$$I^{s}_{A,2} = g(|\widetilde{\Delta}_A|^2 + |\eta + Fe^{-i\varphi}|^2), \quad \text{pumping from port 2,} \tag{D12}$$

in which

$$g = \frac{\varepsilon^2}{|\widetilde{\Delta}_A^2 - (\eta + Fe^{-i\varphi})(\eta + Fe^{i\varphi})|^2}. \tag{D13}$$

Considering that G is much smaller than Ω, i.e., $G \ll \Omega$, we can ignore the term $G^2(|a^s_{CW}|^2 + |a^s_{CCW}|^2)/\Omega$ in the following discussion.

Similarly, the steady-state light intensities in resonator B I^s_B ($I^s_B = |b^s_{CW}|^2 + |b^s_{CCW}|^2$) corresponding to pumping from port 1 and port 2 can be obtained, but their specific forms are too cumbersome to list here. Moreover, for the convenience of comparison, we further define

$$\delta I^s_A = I^s_{A,1} - I^s_{A,2} = g(|\eta + Fe^{i\varphi}|^2 - |\eta + Fe^{-i\varphi}|^2) \tag{D14}$$

as the steady-state light intensity difference in resonator A generated by pumping from different ports. Obviously, if time-reversal symmetry holds, i.e., $\varphi = \pi\mathbb{Z}$, where $\mathbb{Z}$ is an arbitrary integer, then $I^s_{A,1} = I^s_{A,2}$ and $\delta I^s_A = 0$; however, if time-reversal symmetry is broken, i.e., $\varphi \neq \pi\mathbb{Z}$, one can easily verify that $I^s_{A,1} \Rightarrow I^s_{A,2}$ and $\delta I^s_A \Rightarrow -\delta I^s_A$ under the transformation of $\varphi \Rightarrow -\varphi$. Such a transformation relation reveals the chirality of the system dynamics on the φ axis.

Finally, it is noteworthy that the steady-state solution predicts several other useful working states of the device. For example, scattering caused by surface defects can be greatly suppressed by one properly selecting the parameters, which is essential for constructing robust communication channels. As illustrated in Eq. (D7), when $\eta + Fe^{i\varphi} \to 0$, the CCW mode in resonator A will be greatly suppressed for pumping from port 1. Similarly, when $\eta + Fe^{-i\varphi} \to 0$, as shown in Eq. (D6), the CW mode in resonator A will be greatly suppressed for pumping from port 2. We note that in the proposed device, by the use of nanopositioning translation stages and fiber tips, J, γ, η, κ, $|\xi|$, and φ can be continuously tuned over a wide range. Therefore, the conditions $\eta + Fe^{i\varphi} \to 0$ and $\eta + Fe^{-i\varphi} \to 0$ are both achievable. More discussion on this aspect is beyond the scope of this work and will be conducted in the future.

APPENDIX E: DETAILS ON CHIRAL CHAOS FOR SENSING

The core of the chiral chaos–based sensing principle lies in constructing the appropriate sensing window. Below, we take the detection of a monochromatic optical weak signal as an example to demonstrate the performance of the sensing window. More complicated cases, e.g., weak signals which are not monochromatic or embedded in the background noise, will be discussed in follow-up work. The specific form of the monochromatic weak signal is

$$s(\tau) = \delta\varepsilon \cos[(\omega + \delta\omega)\tau + \theta], \quad \delta\varepsilon = \sqrt{\frac{\kappa_0 p_s}{\hbar(\omega + \delta\omega)}}, \tag{E1}$$

in which $\delta\varepsilon$, $\omega + \delta\omega$, and p_s are the amplitude, frequency, and power of the weak signal, respectively, ω and ε ($\varepsilon \gg \delta\varepsilon$) are the frequency and amplitude of the pumping field, respectively, θ and $\delta\omega$ represent the initial phase difference and the detuning between the signal and the pumping field, respectively, κ_0 is the taper-resonator coupling rate, and $\tau = \Omega t$ is the extended timescale. To simplify the discussion and facilitate experimental verification, we assume that the weak signal is directly loaded into the pumping field. Then the equivalent Hamiltonian is ($\hbar = 1$)

$$\hat{H} = \begin{cases} i\left[\varepsilon + \delta\varepsilon e^{-i(\delta\omega\tau+\theta)}\right]\hat{a}^{\dagger}_{CW} - i\left[\varepsilon + \delta\varepsilon e^{i(\delta\omega\tau+\theta)}\right]\hat{a}_{CW}, & \text{pumping from port 1,} \\ i\left[\varepsilon + \delta\varepsilon e^{-i(\delta\omega\tau+\theta)}\right]\hat{a}^{\dagger}_{CCW} - i\left[\varepsilon + \delta\varepsilon e^{i(\delta\omega\tau+\theta)}\right]\hat{a}^{\dagger}_{CCW}, & \text{pumping from port 2,} \end{cases} \tag{E2}$$

where a rotating frame at frequency ω and the rotating-wave approximation have been applied.

For more intuitive comparison, we now use the sensing results obtained by pumping from port 2 of the device to simulate the performance of the conventional chaos-based sensing proposal. Note that switching the pumping port has no effect on the sensing performance of the conventional reciprocal chaotic sensor; however, for the chiral chaotic sensor, the situation is different. By using the sensing window, we superimpose the contributions from the two pumping ports to obtain the final sensing result (success or failure), as shown in Fig. 4.

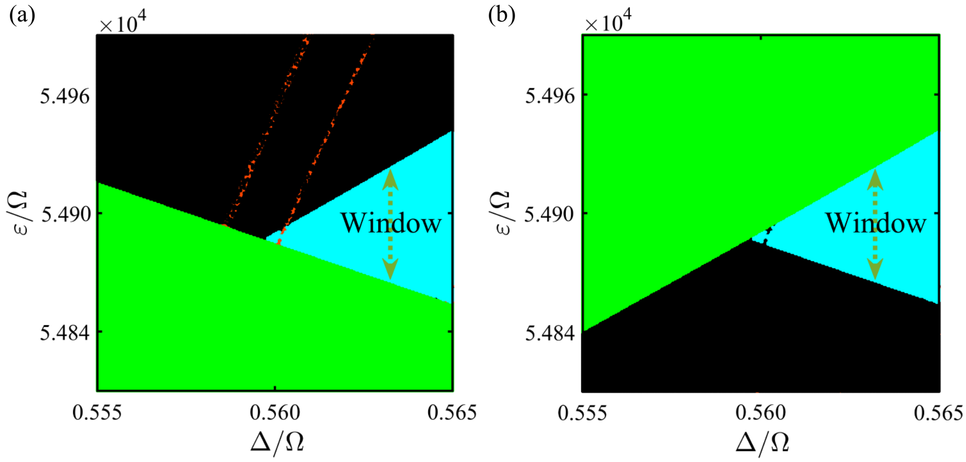

FIG. 9. (a),(b) Phase diagrams of the device in the selected parameter regions, where (a),(b) correspond to pumping from port 1 and port 2, respectively. Green, red, and black regions denote self-induced-oscillation, period-doubling-bifurcation, and chaotic regimes, respectively. The cyan region denotes a special type of chaotic regime, i.e., the sensing window regime. In this regime, the device works in the chaotic state, no matter from which port the pumping is applied. Moreover, a perturbation with strength $\delta\varepsilon$ may induce the chaos-order transition, when the device works in the sensing window regime. The parameters are as follows [22]: $\Delta_A = \Delta_B = \Delta$, $\delta\varepsilon = 0$, $\varphi/\pi = 0.5$, and $|\xi|/\Omega = 5$, with the other parameters being the same as in Fig. 2.

Before testing, we first construct an appropriate sensing window on the (ε, ω) plane. We point out that the sensing windows do not appear in isolation, and they will present a continuous sensing window regime in phase diagrams. As shown in Fig. 9, the two phase diagrams of the device corresponding to the two different pumping ports are different. Therefore, we can construct sensing window regimes on phase diagrams. In such regimes, the working state of the device is sensitive only to the strength of the weak signal, and the sensitivity will not be affected by the randomness of certain parameters in the detected signals. For example, the cyan region shown in Fig. 9 is a sensing window regime.

For the cyan region, the device operates in the chaotic state, no matter from which port the pumping is applied. In addition, for the resonance ($\delta\omega = 0$) or near-resonance ($\delta\omega/\omega \ll 1$) weak signals with amplitude $|\delta\varepsilon|$, even if the value of θ is random, the working state of the device can still undergo a chaos-to-order transition. If $\theta \in (0, \pi/2)$, the chaos-to-order transition can be induced for pumping from port 2; if $\theta \in (\pi/2, \pi)$, the chaos-to-order transition can be induced for pumping from port 1. As illustrated in the bidirectional arrows in Fig. 9, each vertical parameter stripe in the cyan region can be constructed as a sensing window. The half-width D and the center position P of the sensing windows are determined by the upper and lower boundaries. It is obvious that the distance between the upper and lower boundaries of the cyan region varies slowly (without abrupt changes). Therefore, the parameters of the sensing windows can be adjusted smoothly over a wide range. This indicates that the application fields of the sensing window regimes are broad. Narrow windows are suitable for sensitive sensing, while wide windows are suitable for threshold alarms [66]. In Fig. 5, the sensing window regime constructed on the (ε, ω) plane is the cyan region in Fig. 9, and the working point F is selected as $\varepsilon/\Omega = 54887$ and $\Delta/\Omega = 0.5598$.

[1] M. Inaki, J. Liu, and K. Matsuno, Cell chirality: Its origin and roles in left-right asymmetric development, Phil. Trans. R. Soc. B **371**, 20150403 (2016).
[2] L. A. Nguyen, H. He, and C. Pham-Huy, Chiral drugs: An overview, Int. J. Biomed. Sci. **2**, 85 (2006).
[3] J. R. Brandt, F. Salerno, and M. J. Fuchter, The added value of small-molecule chirality in technological applications, Nat. Rev. Chem. **1**, 0045 (2017).
[4] R. A. Reddy and C. Tschierske, Bent-core liquid crystals: Polar order, superstructural chirality and spontaneous desymmetrisation in soft matter systems, J. Mater. Chem. **16**, 907 (2006).
[5] H.-W. Hammer, S. König, and U. van Kolck, Nuclear effective field theory: Status and perspectives, Rev. Mod. Phys. **92**, 025004 (2020).
[6] P. Lodahl, S. Mahmoodian, S. Stobbe, A. Rauschenbeutel, P. Schneeweiss, J. Volz, H. Pichler, and P. Zoller, Chiral quantum optics, Nature **541**, 473 (2017).
[7] H. Cao and J. Wiersig, Dielectric microcavities: Model systems for wave chaos and non-Hermitian physics, Rev. Mod. Phys. **87**, 61 (2015).
[8] S. H. Yang, R. Naaman, Y. Paltiel, and S. S. P. Parkin, Chiral spintronics, Nat. Rev. Phys. **3**, 328 (2021).
[9] A. Lininger, G. Palermo, A. Guglielmelli, G. Nicoletta, M. Goel, M. Hinczewski, and G. Strangi, Chirality in light-matter interaction, Adv. Mater. **35**, 2107325 (2022).
[10] M. Schäferling, *Chiral Nanophotonics* (Springer International Publishing, Switzerland, 2017).

[11] D. Ayuso, O. Neufeld, A. F. Ordonez, P. Decleva, G. Lerner, O. Cohen, M. Ivanov, and O. Smirnova, Synthetic chiral light for efficient control of chiral light-matter interaction, Nat. Photonics **13**, 866 (2019).
[12] G. Tkachenko and E. Brasselet, Optofluidic sorting of material chirality by chiral light, Nat. Commun. **5**, 3577 (2014).
[13] J. B. Pendry, A chiral route to negative refraction, Science **306**, 1353 (2004).
[14] M. Scheucher, A. Hilico, E. Will, J. Volz, and A. Rauschenbeutel, Quantum optical circulator controlled by a single chirally coupled atom, Science **354**, 1577 (2016).
[15] R. Sarma, L. Ge, J. Wiersig, and H. Cao, Rotating optical microcavities with broken chiral symmetry, Phys. Rev. Lett. **114**, 053903 (2015).
[16] A. C. Newell and J. V. Moloney, *Nonlinear Optics* (Addison-Wesley, Redwood City, 1992).
[17] S. H. Strogatz, *Nonlinear Dynamics and Chaos: With Applications to Physics, Biology, Chemistry, and Engineering* (Westview Press, Boca Raton, 2015).
[18] M. A. Lemonde, N. Didier, and A. A. Clerk, Nonlinear interaction effects in a strongly driven optomechanical cavity, Phys. Rev. Lett. **111**, 053602 (2013).
[19] F. Monifi, J. Zhang, Ş. K. Özdemir, B. Peng, Y. X. Liu, F. Bo, F. Nori, and L. Yang, Optomechanically induced stochastic resonance and chaos transfer between optical fields, Nat. Photonics **10**, 399 (2016).
[20] L. Bakemeier, A. Alvermann, and H. Fehske, Route to chaos in optomechanics, Phys. Rev. Lett. **114**, 013601 (2015).
[21] T. Carmon, M. C. Cross, and K. J. Vahala, Chaotic quivering of micron-scaled on-chip resonators excited by centrifugal optical pressure, Phys. Rev. Lett. **98**, 167203 (2007).
[22] M. Aspelmeyer, T. J. Kippenberg, and F. Marquardt, Cavity optomechanics, Rev. Mod. Phys. **86**, 1391 (2014).
[23] D.-W. Zhang, C. You, and X.-Y. Lü, Intermittent chaos in cavity optomechanics, Phys. Rev. A **101**, 053851 (2020).
[24] D.-W. Zhang, L.-L. Zheng, C. You, C.-S. Hu, Y. Wu, and X.-Y. Lü, Nonreciprocal chaos in a spinning optomechanical resonator, Phys. Rev. A **104**, 033522 (2021).
[25] X.-Y. Lü, H. Jing, J.-Y. Ma, and Y. Wu, $\mathcal{PT}$-symmetry-breaking chaos in optomechanics, Phys. Rev. Lett. **114**, 253601 (2015).
[26] F. Huang, L. Chen, L. Huang, J. Huang, G. Liu, Y. Chen, Y. Luo, and Z. Chen, Tunable anti-parity-time-symmetric chaos in optomechanics, Phys. Rev. A **104**, L031503 (2021).
[27] D. Navarro-Urrios, N. E. Capuj, M. F. Colombano, P. D. García, M. Sledzinska, F. Alzina, A. Griol, A. Martínez, and C. M. Sotomayor-Torres, Nonlinear dynamics and chaos in an optomechanical beam, Nat. Commun. **8**, 14965 (2017).
[28] V. B. Braginsky and A. B. Manukin, *Measurement of Weak Forces in Physics Experiments* (University of Chicago Press, Chicago, 1977).
[29] V. B. Braginsky and F. Y. Khalili, *Quantum Measurement* (Cambridge University Press, Cambridge, England, 1992).
[30] M. Sciamanna and K. A. Shore, Physics and applications of laser diode chaos, Nat. Photonics **9**, 151 (2015).
[31] F. Verhulst, *Nonlinear Differential Equations and Dynamical Systems* (Springer, Berlin, 2006).
[32] N. Boechler, G. Theocharis, and C. Daraio, Bifurcation-based acoustic switching and rectification, Nat. Mater. **10**, 665 (2011).
[33] G. Y. Wang, D. J. Chen, J. Y. Lin, and X. Chen, The application of chaotic oscillators to weak signal detection, IEEE Trans. Ind. Electron. **46**, 440 (1999).
[34] T. Karimov, E. G. Nepomuceno, O. Druzhina, A. Karimov, and D. Butusov, Chaotic oscillators as inductive sensors: Theory and practice, Sensors **19**, 4314 (2019).
[35] T. Shinbrot, C. Grebogi, J. A. Yorke, and E. Ott, Using small perturbations to control chaos, Nature **363**, 411 (1993).
[36] M. A. F. Sanjuán and C. Grebogi, *Recent Progress in Controlling Chaos* (Wold Scientific, Singapore, 2010).
[37] J. M. González-Miranda, *Synchronization and Control of Chaos* (Imperial College Press, London, 2004).
[38] M. R. Foreman, J. D. Swaim, and F. Vollmer, Whispering gallery mode sensors, Adv. Opt. Photonics **7**, 168 (2015).
[39] Y. L. Liu, C. Wang, J. Zhang, and Y.-x. Liu, Cavity optomechanics: Manipulating photons and phonons towards the single-photon strong coupling, Chin. Phys. B **27**, 024204 (2018).
[40] Y. F. Jiao, S. D. Zhang, Y. L. Zhang, A. Miranowicz, L. M. Kuang, and H. Jing, Nonreciprocal optomechanical entanglement against backscattering losses, Phys. Rev. Lett. **125**, 143605 (2020).
[41] Z.-P. Liu, J. Zhang, Ş. K. Özdemir, B. Peng, H. Jing, X.-Y. Lü, C.-W. Li, L. Yang, F. Nori, and Y.-x. Liu, Metrology with $\mathcal{PT}$-symmetric cavities: enhanced sensitivity near the $\mathcal{PT}$-phase transition, Phys. Rev. Lett. **117**, 110802 (2016).
[42] B. Peng, Ş. K. Özdemir, S. Rotter, H. Yilmaz, M. Liertzer, F. Monifi, C. M. Bender, F. Nori, and L. Yang, Loss-induced suppression and revival of lasing, Science **346**, 328 (2014).
[43] S. Kim, J. M. Taylor, and G. Bahl, Dynamic suppression of Rayleigh backscattering in dielectric resonators, Optica **6**, 1016 (2019).
[44] W. J. Chen, Ş. K. Özdemir, G. M. Zhao, J. Wiersig, and L. Yang, Exceptional points enhance sensing in an optical microcavity, Nature **548**, 192 (2017).
[45] Y. L. Chen, W. L. Jin, Y. F. Xiao, and X. M. Zhang, Measuring the charge of a single dielectric nanoparticle using a high-Q optical microresonator, Phys. Rev. Applied **6**, 044021 (2016).
[46] Ş. K. Özdemir, S. Rotter, F. Nori, and L. Yang, Parity-time symmetry and exceptional points in photonics, Nat. Mater. **18**, 783 (2019).
[47] M. Ludwig and F. Marquardt, Quantum many-body dynamics in optomechanical arrays, Phys. Rev. Lett. **111**, 073603 (2013).
[48] A. Mari and J. Eisert, Gently modulating optomechanical systems, Phys. Rev. Lett. **103**, 213603 (2009).
[49] Y. H. Lai, Y. K. Lu, M. G. Suh, Z. Q. Yuan, and K. Vahala, Observation of the exceptional-point-enhanced Sagnac effect, Nature **576**, 65 (2019).
[50] H. G. Schuster and W. Just, *Deterministic Chaos* (Wiley-VCH, Weinheim, 2005).
[51] J. Zhang, B. Peng, S. Kim, F. Monifi, X. F. Jiang, Y. H. Li, P. Yu, L. Q. Liu, Y. X. Liu, A. Alù, and L. Yang, Optomechanical dissipative solitons, Nature **600**, 75 (2021).

[52] J. Koch, A. A. Houck, K. L. Hur, and S. M. Girvin, Time-reversal-symmetry breaking in circuit-QED-based photon lattices, Phys. Rev. A **82**, 043811 (2010).
[53] L. Q. Yuan, Q. Lin, A. W. Zhang, M. Xiao, X. F. Chen, and S. H. Fan, Photonic gauge potential in one cavity with synthetic frequency and orbital angular momentum dimensions, Phys. Rev. Lett. **122**, 083903 (2019).
[54] M. Hafezi, E. A. Demler, M. D. Lukin, and J. M. Taylor, Robust optical delay lines with topological protection, Nat. Phys. **7**, 907 (2011).
[55] M. Hafezi, S. Mittal, J. Fan, A. Migdall, and J. M. Taylor, Imaging topological edge states in silicon photonics, Nat. Photonics **7**, 1001 (2013).
[56] Y. Chen, Y. L. Zhang, Z. Shen, C. L. Zou, G. C. Guo, and C. H. Dong, Synthetic gauge fields in a single optomechanical resonator, Phys. Rev. Lett. **126**, 123603 (2021).
[57] M. C. Gutzwiller, *Chaos in Classical and Quantum Mechanics* (Springer, New York, 1990).
[58] A. B. Harris, R. D. Kamien, and T. C. Lubensky, Molecular chirality and chiral parameters, Rev. Mod. Phys. **71**, 1745 (1999).
[59] M. Creutz, Aspects of chiral symmetry and the lattice, Rev. Mod. Phys. **73**, 119 (2001).
[60] G. Benettin, L. Galgani, A. Giorgilli, and J. M. Strelcyn, Lyapunov characteristic exponents for smooth dynamical systems and for Hamiltonian systems; a method for computing all of them. Part 1: Theory, Meccanica **15**, 9 (1980).
[61] A. Wolf, J. B. Swift, H. L. Swinney, and J. A. Vastano, Determining Lyapunov exponents from a time-series, Physica D **16**, 285 (1985).
[62] J. G. Wu, S. W. Huang, Y. J. Huang, H. Zhou, J. H. Yang, J. M. Liu, M. B. Yu, G. Q. Lo, D. L. Kwong, S. K. Duan, and C. W. Wong, Mesoscopic chaos mediated by Drude electron-hole plasma in silicon optomechanical oscillators, Nat. Commun. **8**, 15570 (2017).
[63] W. Yang, A. Joshi, and M. Xiao, Chaos in an electromagnetically induced transparent medium inside an optical cavity, Phys. Rev. Lett. **95**, 093902 (2005).
[64] S. Sunada, S. Shinohara, T. Fukushima, and T. Harayama, Signature of wave chaos in spectral characteristics of microcavity lasers, Phys. Rev. Lett. **116**, 203903 (2016).
[65] J. G. Zhu, Ş. K. Özdemir, L. N. He, and L. Yang, Controlled manipulation of mode splitting in an optical microcavity by two Rayleigh scatterers, Opt. Express **18**, 23535 (2010).
[66] J. S. Wilson, *Sensor Technology Handbook* (Elsevier, Oxford, 2005).
[67] J. Wiersig, Enhancing the sensitivity of frequency and energy splitting detection by using exceptional points: Application to microcavity sensors for single-particle detection, Phys. Rev. Lett. **112**, 203901 (2014).
[68] W. W. Chow and S. Wieczorek, Using chaos for remote sensing of laser radiation, Opt. Express **17**, 7491 (2009).
[69] B. J. Privett, J. H. Shin, and M. H. Schoenfisch, Electrochemical sensors, Anal. Chem. **82**, 4723 (2010).
[70] A. Demir, Nonlinear phase noise in optical-fiber-communication systems, J. Light. Technol. **25**, 8 (2007).
[71] R. Slavík, F. Parmigiani, J. Kakande, C. Lundström, M. Sjödin, P. A. Andrekson, R. Weerasuriya, S. Sygletos, A. D. Ellis, L. G. Nielsen, D. Jakobsen, S. Herstrøm, R. Phelan, J. O'Gorman, A. Bogris, D. Syvridis, S. Dasgupta, P. Petropoulos, and D. J. Richardson, All-optical phase and amplitude regenerator for next-generation telecommunications systems, Nat. Photonics **4**, 10 (2010).
[72] E. Ott, C. Grebogi, and J. A. Yorke, Controlling chaos, Phys. Rev. Lett. **64**, 1196 (1990).
[73] A. Osada, R. Hisatomi, A. Noguchi, Y. Tabuchi, R. Yamazaki, K. Usami, M. Sadgrove, R. Yalla, M. Nomura, and Y. Nakamura, Cavity optomagnonics with spin-orbit coupled photons, Phys. Rev. Lett. **116**, 223601 (2016).
[74] S. Maayani, R. Dahan, Y. Kligerman, E. Moses, A. U. Hassan, H. Jing, F. Nori, D. N. Christodoulides, and T. Carmon, Flying couplers above spinning resonators generate irreversible refraction, Nature **558**, 569 (2018).
[75] J. G. Zhu, S. K. Ozdemir, Y. F. Xiao, L. Li, L. N. He, D. R. Chen, and L. Yang, On-chip single nanoparticle detection and sizing by mode splitting in an ultrahigh-Q microresonator, Nat. Photonics **4**, 46 (2010).
[76] X. M. Zhang, H. S. Choi, and A. M. Armani, Ultimate quality factor of silica microtoroid resonant cavities, Appl. Phys. Lett. **96**, 153304 (2010).
[77] I. S. Grudinin, H. Lee, O. Painter, and K. J. Vahala, Phonon laser action in a tunable two-level system, Phys. Rev. Lett. **104**, 083901 (2010).
[78] T. J. Kippenberg, S. M. Spillane, and K. J. Vahala, Kerr-nonlinearity optical parametric oscillation in an ultrahigh-Q toroid microcavity, Phys. Rev. Lett. **93**, 083904 (2004).
[79] C. Bekker, C. G. Baker, R. Kalra, H. H. Cheng, B. B. Li, V. Prakash, and W. P. Bowen, Free spectral range electrical tuning of a high quality on-chip microcavity, Opt. Express **26**, 33649 (2018).
[80] A. Mazzei, S. Götzinger, L. de S. Menezes, G. Zumofen, O. Benson, and V. Sandoghdar, Controlled coupling of counterpropagating whispering-gallery modes by a single Rayleigh scatterer: A classical problem in a quantum optical light, Phys. Rev. Lett. **99**, 173603 (2007).
[81] X. Gu, A. F. Kockum, A. Miranowicz, Y. X. Liu, and F. Nori, Microwave photonics with superconducting quantum circuits, Phys. Rep. **718–719**, 1 (2017).
[82] N. R. Bernier, L. D. Tóth, A. Koottandavida, M. A. Ioannou, D. Malz, A. Nunnenkamp, A. K. Feofanov, and T. J. Kippenberg, Nonreciprocal reconfigurable microwave optomechanical circuit, Nat. Commun. **8**, 604 (2017).
[83] L. B. Shao, W. B. Mao, S. Maity, N. Sinclair, Y. W. Hu, L. Yang, and M. Loncar, Non-reciprocal transmission of microwave acoustic waves in nonlinear parity-time symmetric resonators, Nat. Electron. **3**, 267 (2020).
[84] A. Noguchi, R. Yamazaki, Y. Tabuchi, and Y. Nakamura, Single-photon quantum regime of artificial radiation pressure on a surface acoustic wave resonator, Nat. Commun. **11**, 1183 (2020).